Physical Review E **68** (2003) 041204 (*19 pages*)

Viscosity in molecular dynamics with periodic boundary conditions

S. Viscardy and P. Gaspard
Center for Nonlinear Phenomena and Complex Systems,
Faculté des Sciences, Université Libre de Bruxelles,
Campus Plaine, Code Postal 231, B-1050 Brussels, Belgium

We report a study of viscosity by the method of Helfand moment in systems with periodic boundary conditions. We propose a new definition of Helfand moment which takes into account the minimum image convention used in molecular dynamics with periodic boundary conditions. Our Helfand-moment method is equivalent to the method based on the Green-Kubo formula and is not affected by ambiguities due to the periodic boundary conditions. Moreover, in hard-ball systems, our method is equivalent to the one developed by B. J. Alder, D. M. Gass, and T. E. Wainwright [*J. Chem. Phys.* **53**, 3813 (1970)]. We apply and verify our method in a fluid composed of $N \geq 2$ hard disks in elastic collisions. We show that the viscosity coefficients already take values in good agreement with Enskog's theory for $N = 2$ hard disks in a hexagonal geometry.

I. INTRODUCTION

Viscosity is the fundamental mechanism of dissipation of momentum in a fluid. Viscosity is described at the macroscopic level by the Navier-Stokes equations which are the equations of balance of momentum in a fluid. At the microscopic level, viscosity arises because of a transfer of momentum between fluid layers moving at different velocities as already explained by Maxwell thanks to kinetic theory.

In the fifties, Green, Kubo, Mori, and others provided an explanation of all the transport properties in terms of time-dependent statistical correlations of microscopic currents associated with each transport property [1–4]. They showed that the transport coefficients are given as the time integrals of the time autocorrelation functions of the microscopic currents, yielding the famous Green-Kubo formulas. Thereafter, Helfand showed in the early sixties that the transport coefficients can be expressed by Einstein-like formulas in terms of moments – the so-called Helfand moments – which are the time integrals of the microscopic currents [5].

These new methods by Green, Kubo, Mori, Helfand, and others have been applied to the computation of transport properties by molecular-dynamics simulations, in particular, by Alder *et al.* [6]. In molecular-dynamics simulations, the system is necessarily composed of a finite number of particles which are usually moving in a domain defined with periodic boundary conditions in order to simulate the bulk properties. The periodic boundary conditions (p.b.c.) usually considered in molecular dynamics are based on the so-called *minimum image convention* according to which interaction should occur between pairs of particles separated by the minimum distance among the infinitely many images of the particles allowed by the p.b.c.. In molecular-dynamics simulations, the minimum image convention plays a fundamental role to define the microscopic current entering the Green-Kubo formula.

We may wonder if the Helfand-moment method could be applied to molecular dynamics simulations with p.b.c.. The advantage of the Helfand-moment method is that it expresses the transport coefficients by Einstein-like formulas, directly showing their positivity. Moreover, this method is very efficient because it is based on a straightforward accumulation which is numerically robust. Actually, it is a Helfand-moment method which has been numerically implemented by Alder *et al.* for viscosity in hard-ball fluids [6]. Several other implementations of the Helfand-moment method have been considered and discussed in the literature [7–9]. However, the implementation of this method for systems subject to p.b.c. other than hard-ball fluids seems to remain ambiguous as reported by Erpenbeck in Ref. [9].

The purpose of the present paper is to propose a Helfand-moment method which is appropriate for molecular dynamics simulations with p.b.c. and which is strictly equivalent to calculations with the Green-Kubo formula. For this purpose, we show the need to take into account the minimum image convention. In this way, we are able to obtain a Helfand moment giving viscosity thanks to an Einstein-like formula in molecular dynamics with p.b.c.. The so-obtained value of viscosity is in full agreement with the value of the Green-Kubo formula and also with the value obtained by Alder *et al.* [6].

Our method is applied to the hard-disk fluid. We study in detail the simple model composed of two hard disks in elastic collisions in a domain defined by p.b.c.. Due to the defocusing character of the disks, this model is chaotic. Bunimovich and Spohn have demonstrated that the viscosity already exists in this system with only two particles [10]. The model they studied is defined with p.b.c. in a square geom-

etry. It presents a fluid and a solid phases which are separated by a phase transition. The problems presented by the model in a square geometry are that: (*i*) the viscosity exists only in the solid phase; (*ii*) the viscosity tensor which is of fourth order is *anisotropic* on a square lattice. In the present work, we solve these problems by considering a hexagonal geometry. Indeed, in the hexagonal geometry, the fourth-order viscosity tensor is isotropic and we can proof the existence of viscosity already in the fluid phase.

Furthermore, we apply our method to systems containing more and more hard disks. We show that the values of the shear viscosity obtained by our Helfand-moment method are in good agreement with Enskog's theory, already for the fluid of two-hard disks.

The paper is organized as follows. In Sec. II, we derive our expression of the Helfand moment for the viscosity tensor to be of application in molecular-dynamics simulations with p.b.c.. In Sec. III, we describe the model of two hard disks in the hexagonal and square geometries. In Sec. IV, we study different properties of the model like the mean free path and the hydrostatic pressure, in particular, across the fluid-solid phase transition. In Sec. V, the Helfand-moment method is applied to the two-disk model to calculate the shear and bulk viscosities. We show how the fluid-solid phase transition affects the viscosities in this model. In Sec. VI, we extend our results to systems with $N = 4, 8, 12, ..., 40$ hard disks. We show that the shear viscosity already takes a value in good agreement with Enskog's theory in the two-hard-disk system. Our results are discussed and conclusions are drawn in Sec. VII.

II. HYDRODYNAMICS, HELFAND MOMENT, AND VISCOSITY

A. Viscosity and hydrodynamics

The hydrodynamic theory provides us with the equations of motion for the conserved quantities in a fluid. In particular, the local conservation of momentum is expressed by the well-known *Navier-Stokes equations* [11]:

$$\frac{\partial \rho v_i}{\partial t} = -\frac{\partial \Pi_{ij}}{\partial r_j} \ , \tag{1}$$

where

$$\Pi_{ij} = \rho \, v_i v_j + P \, \delta_{ij} - \sigma'_{ij} \ , \tag{2}$$

is the momentum flux density tensor, ρv_i is the momentum density, P the hydrostatic pressure, and σ'_{ij} the viscosity stress tensor. This last tensor takes into account the internal friction occurring in a fluid when different parts of the fluid move with different velocities. Therefore, σ'_{ij} has to be proportional to the space derivatives of the velocities:

$$\sigma'_{ij} = \eta_{ij,kl} \, \frac{\partial v_k}{\partial r_l} \ , \tag{3}$$

where $\eta_{ij,kl}$ is the *viscosity tensor*.

For isotropic systems, the theory of Cartesian tensors shows that the basic isotropic tensor is the Kronecker tensor δ_{ij} and that all the isotropic tensors of even order can be written like a sum of products of tensors δ_{ij} [12]:

$$\eta_{ij,kl} = a \, \delta_{ij} \, \delta_{kl} + b \, \delta_{ik} \, \delta_{jl} + c \, \delta_{jk} \, \delta_{il} \ , \tag{4}$$

where a, b and c are scalars. Since the viscosity stress tensor is symmetric $\sigma'_{ij} = \sigma'_{ji}$, only two of these coefficients are independent because $b = c$. After a rearrangement, we have:

$$\sigma'_{ij} = \eta \left(\frac{\partial v_i}{\partial r_j} + \frac{\partial v_j}{\partial r_i} - \frac{2}{d} \, \delta_{ij} \, \frac{\partial v_l}{\partial r_l} \right) + \zeta \, \delta_{ij} \, \frac{\partial v_l}{\partial r_l} \ , \tag{5}$$

for a d-dimensional system. The coefficients $\eta = b$ and $\zeta = a + (2/d)b$ are respectively the *shear and bulk viscosities* and they can be expressed in terms of the elements of the fourth-order viscosity tensor as:

$$\begin{cases} \eta = \eta_{xy,xy} \ , \\ \zeta = \dfrac{1}{d} \, \eta_{xx,xx} + \dfrac{d-1}{d} \, \eta_{xx,yy} \ . \end{cases} \tag{6}$$

B. The Green-Kubo formula in molecular dynamics with p.b.c.

Several techniques have been developed during the last century to evaluate the transport coefficients. One of the most important methods was established by Green, Kubo, and Mori [1–4]. It consists in having a relation between each transport coefficient and the autocorrelation function of the associated flux or microscopic current. In our case (see Appendix A), we have:

$$\eta_{ij,kl} = \frac{\beta}{V} \int_0^\infty \left[\langle J_{ij}(0)\ J_{kl}(t) \rangle - \langle J_{ij} \rangle \langle J_{kl} \rangle \right]\ dt\ , \tag{7}$$

with the microscopic current:

$$J_{ij}\ =\ \sum_{a=1}^{N} \frac{p_{ai}\ p_{aj}}{m} + \frac{1}{2} \sum_{a \neq b=1}^{N}\ F_i(\mathbf{r}_a - \mathbf{r}_b)\ (r_{aj} - r_{bj})\ , \tag{8}$$

$\mathbf{p}_a$ and $\mathbf{r}_a$ being the momentum and the position of the a^{th} particle, while $\mathbf{F}(\mathbf{r}_a - \mathbf{r}_b)$ is the force between particles a and b. In Eq. (7) the average $\langle \cdot \rangle$ is performed with respect to the equilibrium state. We notice that, for the microcanonical state,

$$\beta = \frac{1}{k_{\rm B} T}\ \frac{N}{N-1}\ , \tag{9}$$

(see Appendix A).

A very important point is that, in a system with p.b.c. as considered in molecular-dynamics simulations, the difference of positions $\mathbf{r}_a - \mathbf{r}_b$ must satisfy the *minimum image convention* that

$$|r_{aj} - r_{bj}| \leq \frac{L}{2}\ , \qquad \text{for}\ \ j = 1, ..., d\ , \tag{10}$$

for a cubic geometry. More generally, the difference of positions must remain within a unit cell of the Bravais lattice used to define the p.b.c.. With p.b.c., there is indeed an infinite lattice of images of each particle. All these images move in parallel. If the force has a finite range the particle a interacts only with the particles b within its interaction range. The force field $\mathbf{F}(\mathbf{r})$ has a finite range of interaction beyond which it vanishes. The interaction range is supposed to be smaller than the size L of the box containing all the particles. It is important to notice that we do not suppose here that the force field is periodic. In order to define a dynamics which is periodic in the box of size L the positions should jump in order to satisfy the minimum image convention. As a consequence of this assumption, the positions and momenta used to calculate the viscosity by the Green-Kubo method actually obey modified Newton's equations

$$\left\{ \begin{array}{l} \dfrac{d\mathbf{r}_a}{dt} = \dfrac{\mathbf{p}_a}{m} + \displaystyle\sum_s \Delta\mathbf{r}_a^{(s)}\ \delta(t - t_s)\ , \\ \dfrac{d\mathbf{p}_a}{dt} = \displaystyle\sum_{b(\neq a)} \mathbf{F}(\mathbf{r}_a - \mathbf{r}_b)\ , \end{array} \right. \tag{11}$$

where $\Delta\mathbf{r}_a^{(s)}$ is the jump of the particle a at time t_s in order to satisfy the minimum image convention. Moreover, we impose that the particle No. 1 does not jump. To satisfy these conditions, the jumps at the time t_s when $|r_{aj}(t_s) - r_{bj}(t_s)| = L/2$ can be given by

$$\text{for}\ \ a < b: \quad \left\{ \begin{array}{ll} \Delta r_{aj}^{(s)} = 0\ , & \\ \Delta r_{bj}^{(s)} = \varepsilon L\ , & \\ \Delta r_{cj}^{(s)} = 0\ , & \text{for}\ \ c \neq a, b\ , \\ \Delta r_{dk}^{(s)} = 0\ , & \text{for}\ \ k \neq j \quad \text{and} \quad \forall d\ , \end{array} \right. \tag{12}$$

with $\varepsilon = \mathrm{sgn}[p_{aj}(t_s) - p_{bj}(t_s)]$. The modified Newton equations (11) define a dynamics which is periodic on the torus of the relative coordinates $\mathbf{r}_a - \mathbf{r}_1$ because the jumps of the relative coordinates are vectors of the Bravais cubic lattice: $\Delta r_{aj}^{(s)} - \Delta r_{1j}^{(s)} = 0, \pm L$, while the momenta $\mathbf{p}_a$ remain functions of the time without singularities worst than discontinuities. We notice that modified Newton's equations (11) conserve energy, total momentum and preserve phase-space volumes (Liouville's theorem).

C. Helfand moment for molecular dynamics with p.b.c.

In the sixties, Helfand has derived quantities associated with the different transport processes, in particular for the viscosities [5]. These new quantities $G_{ij}(t)$ are such that we can obtain an Einstein-like relation for each transport coefficient. For the shear viscosity coefficient, we have:

$$\eta = \lim_{t\to\infty} \frac{\beta}{2tV} \left\langle [G_{xy}(t) - G_{xy}(0)]^2 \right\rangle \ . \tag{13}$$

More generally, we can define such a relation for each element of the viscosity tensor:

$$\eta_{ij,kl} = \lim_{t\to\infty} \frac{\beta}{2tV} \ [\langle G_{ij}(t) G_{kl}(t)\rangle - \langle G_{ij}(t)\rangle\langle G_{kl}(t)\rangle] \tag{14}$$

if we take $G_{ij}(0) = 0$. The *Helfand moment* $G_{ij}(t)$ is defined as the integral of the microscopic current appearing in the Green-Kubo relation:

$$G_{ij}(t) = G_{ij}(0) + \int_0^t J_{ij}(\tau)\ d\tau \ . \tag{15}$$

As a consequence of the definition (15), the Einstein-Helfand formula (14) is equivalent to the Green-Kubo formula (7), as proved in Appendix B. In a system of N particles on a torus and satisfying the minimum image convention, we can integrate the current (8) with modified Newton's equations (11) to get:

$$G_{ij}(t) = \sum_{a=1}^{N} p_{ai}(t)\ r_{aj}(t) - \sum_{a=1}^{N} \sum_{s} p_{ai}^{(s)}\ \Delta r_{aj}^{(s)}\ \theta(t - t_s) \ , \tag{16}$$

where $G_{ij}(0) = 0$, $p_{ai}^{(s)} = p_{ai}(t_s)$ and $\theta(t - t_s)$ is the *Heaviside step function* at the time t_s of the jump s:

$$\theta(t - t_s) = \begin{cases} 1 \ , & \text{for } \ t > t_s \ , \\ 0 \ , & \text{for } \ t < t_s \ . \end{cases} \tag{17}$$

The expression (16) which we propose in the present paper can be used to obtain the viscosity coefficients thanks to the Einstein-like formulas (14) in a molecular dynamics defined on the torus. We emphasize that the expression (16) may apply to systems of particles interacting with a smooth potential under the condition that the range is finite, or to systems of hard balls in elastic collisions. We show in Appendix C that the hydrostatic pressure can also be written in terms of the Helfand moment (16).

Our Helfand-moment method has several theoretical and numerical advantages: (i) It is strictly equivalent to the Green-Kubo method. (ii) The Einstein-like formula (13) or (14) directly show the positivity of the viscosity coefficient or viscosity tensor because t, β, and V are positive. Moreover, the Helfand moments directly obey central limit theorems, expressing the Gaussian character of the dynamical fluctuations in systems with finite viscosity. (iii) Thanks to our expression (16) of the Helfand moment, the viscosity coefficients are given by a straightforward accumulation over the successive jumps s. For a given system with N particles, numerical convergence can be reached in the limit of an arbitrarily large number of jumps s, under conditions of existence of the viscosity coefficients.

By defining the Helfand moment as the integral (15) of the microscopic current for a system with minimum image convention, we obtain the expression (16) which can be used to directly calculate $\Delta G_{ij}(t) = G_{ij}(t) - G_{ij}(0)$ for the Einstein-Helfand relation, remaining consistent with the requirements imposed by the periodic boundary conditions and with the Green-Kubo formula for a system satisfying the minimum image convention.

D. Comparison with other methods

In the seventies, Alder et al. [6] calculated the viscosity coefficients of hard-ball systems with Einstein-like formulas based on expressions for Helfand moments which are specific to hard-ball systems. Instead of adding a new quantity to the Helfand moment at each passage through the boundaries of the minimum image convention as in Eq. (16), their expression takes into account only the elastic collisions between the hard balls. The Helfand moment can be

obtained by direct integration of the microscopic current according to Eq. (15) with $G_{ij}(0) = 0$:

$$G_{ij}(t) = \int_0^t d\tau \; J_{ij}(\tau) \tag{18}$$

$$= \int_0^t d\tau \left[\sum_{a=1}^{N} \frac{p_{ai} p_{aj}}{m} + \frac{1}{2} \sum_{a \neq b} F_i(\mathbf{r}_a - \mathbf{r}_b) \; (r_{aj} - r_{bj}) \right] . \tag{19}$$

Between the collisions the trajectory is a straight line and the particle velocities change only at each collision. Therefore, the first term in the integral, the kinetic term, is constant during two successive collisions and changes only at the collisions. The second term, the potential term, vanishes between two successive collisions and contributes only at collisions. Indeed, for a hard-ball potential, the forces between the particles a and b colliding at the time t_c of the collision c can be written in terms of the change $\Delta \mathbf{p}_a^{(c)} = \mathbf{p}_a(t_c + \epsilon) - \mathbf{p}_a(t_c - \epsilon)$ of momentum of the particle a at the collision c as

$$\begin{cases} \mathbf{F}\left(\mathbf{r}_a - \mathbf{r}_b\right) = +\Delta \mathbf{p}_a^{(c)} \; \delta(t - t_c) \; , \\ \mathbf{F}\left(\mathbf{r}_b - \mathbf{r}_a\right) = -\Delta \mathbf{p}_a^{(c)} \; \delta(t - t_c) \; , \end{cases} \tag{20}$$

for $t_c - \epsilon < t < t_c + \epsilon$, because $\Delta \mathbf{p}_b^{(c)} = -\Delta \mathbf{p}_a^{(c)}$. The forces with the other particles which are not engaged in the collision vanish. Therefore, we obtain:

$$G_{ij}(t) = \sum_{(c-1,c)} \left(\sum_{a=1}^{N} \frac{p_{ai} p_{aj}}{m} \right)_{(c-1,c)} \Delta t_{c-1,c} + \sum_c \Delta p_{ai}^{(c)} \; r_{abj}^{(c)} \; \theta(t - t_c) \; , \tag{21}$$

where, in the first term, $\Delta t_{c-1,c}$ is the time of flight between the collisions $c-1$ and c during which the momenta remain constant and, in the second term, a and b denote the particles interacting at the collision c and $r_{abj}^{(c)} = r_{aj}(t_c) - r_{bj}(t_c)$. The first sum runs over the intercollisional free flights $(c-1, c)$ between the initial time $t = 0$ and the current time t, while the second sum runs over the collisions occurring between the time $t = 0$ and t. If C denotes the last collision before the current time t, we notice that the last term of the first sum is $\Delta t_{C,C+1} = t - t_C$. Hence, if we differentiate Eq. (21) with respect to time and use (20) we recover the microscopic current (8). Therefore, the expression (21) is equivalent to our expression (16) in the case of hard-ball systems. However, our expression (16) extends to systems with a smooth interaction potential.

A comment is here in order about another method which has been considered and discussed in the literature [7–9]. This other method implements an expression printed in the middle of a presentation given in Ref. [13] for the calculation of shear viscosity with the Helfand-moment method. This expression differs from the Helfand moment by the mere exchange of a square and a sum over the particles. The equivalence of the expression in Ref. [13] with the Helfand moment depends on the vanishing of some cross terms as pointed out in Ref. [7]. Numerical evidence has been obtained in Refs. [8, 9] that the expression in Ref. [13] is in general not valid to calculate the shear viscosity. We notice that both the original Helfand moment and the expression in Ref. [13] do not strictly apply to systems subject to p. b. c. (see discussions in Refs. [8, 9]). This problem is solved by the expression (21) of Ref. [6] in the case of hard-ball fluids and by our expression (16) in the general case.

E. Symmetry considerations in two-dimensional systems

By symmetry, most of the elements of the viscosity tensor are either equal or vanish. First, we have:

$$\eta_{ij,kl} = \eta_{kl,ij} = \eta_{ji,kl} = \eta_{ij,lk} \; , \tag{22}$$

because of the stationarity of the equilibrium average, the reversibility of the microscopic equations, and the fact that $\mathbf{F}(\mathbf{r}_a - \mathbf{r}_b) = \mathbf{F}(\|\mathbf{r}_a - \mathbf{r}_b\|)$ is a central force. Secondly, in our work, the fluid is invariant under rotations by $\varphi = \frac{\pi}{3}$ for the hexagonal geometry and by $\varphi = \frac{\pi}{2}$ for the square one. If we define the viscosity tensor as a linear operator $\hat{\eta}$ acting on matrices A according to $(\hat{\eta}\mathsf{A})_{ij} = \eta_{ij,kl} \; A_{kl}$. Then our discrete symmetry can be written as:

$$\hat{\eta}(\mathsf{R}^{-1}\mathsf{A}R) = \mathsf{R}^{-1}(\hat{\eta}\mathsf{A})\mathsf{R} \; , \tag{23}$$

for all matrices A, R being the rotation matrix

$$\mathsf{R} = \begin{pmatrix} \cos\varphi & -\sin\varphi \\ \sin\varphi & \cos\varphi \end{pmatrix} , \tag{24}$$

and φ is equal to $\frac{\pi}{3}$ or $\frac{\pi}{2}$ respectively for the hexagonal or square systems. Thanks to this symmetry, the only nonvanishing elements are $\eta_{ij,ij} = \eta_{ji,ij}$ and $\eta_{ii,ii} = \eta_{jj,jj}$. Furthermore, for $i \neq j$, $k \neq l$,

$$\eta_{ij,ij} = \eta_{kl,kl} , \qquad \eta_{ii,ii} = \eta_{jj,jj} , \qquad \eta_{ii,jj} = \eta_{kk,ll} . \tag{25}$$

Hence, there are in fact only three independent elements: $\eta_{xx,xx}$, $\eta_{xy,xy}$, $\eta_{xx,yy}$. On the other hand, for an isotropic system, we can see that:

$$\eta = \eta_{xy,xy} , \tag{26}$$

$$\zeta = \frac{1}{2} \left(\eta_{xx,xx} + \eta_{xx,yy} \right) . \tag{27}$$

The third element $\eta_{xx,yy}$ is in fact a combination of the two other elements:

$$\eta_{xx,yy} = \eta_{xx,xx} - 2\, \eta_{xy,xy} . \tag{28}$$

III. DESCRIPTION OF THE TWO-HARD-DISK MODEL

In the present work, we apply our method to a simple model which we describe in the present section. The model is composed of two hard disks in elastic collisions on a torus. Bunimovich and Spohn have previously studied this model for a square geometry [10]. By periodicity, the system extends to a two-dimensional lattice made of infinitely many images of the two disks. For p. b. c. on a square domain, the infinite images form a square lattice, in which each cell contains two disks (see Fig. 1b).

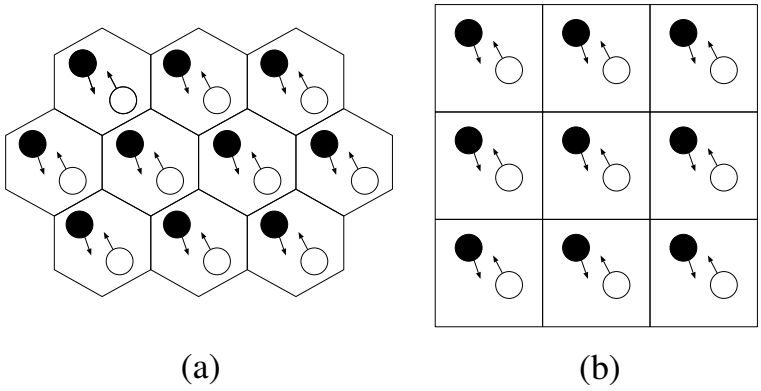

FIG. 1: The model of two hard disks: (a) in the hexagonal geometry and (b) in the square geometry.

In the present work, we generalize this model to the hexagonal geometry (see Fig.1a). The possibility of such a model was pointed out in Ref. [14]. The images of each disk form now a triangular lattice. The two disks (the white and the black ones) have the same diameter σ and mass m. They follow different trajectories. All the black disks move together and all the white ones move together. The system is periodic and the dynamics of the disks can be reduced to the dynamics in the unit cell or torus.

A. Hexagonal geometry

Let us first introduce some parameters of the system. L is the distance between the centers of two neighboring cells. It also corresponds to the distance between two opposite boundaries of a cell.

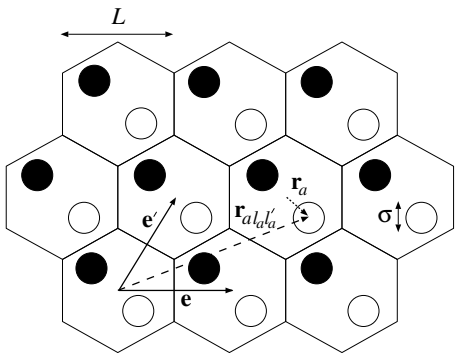

FIG. 2: Basis vector ($\mathbf{e}$ and $\mathbf{e}'$), position vector $\mathbf{r}_a$ of particle a in the cell and the position vector $\mathbf{r}_{a\, l_a\, l'_a}$ in the lattice.

By a linear combination of two vectors:

$$\begin{cases} \mathbf{e} = (L, 0) \ , \\ \mathbf{e}' = \left(\frac{1}{2} L, \frac{\sqrt{3}}{2} L \right) \ , \end{cases} \tag{29}$$

we can spot all the cells of the lattice and then localize the center of a disk thanks to:

$$\mathbf{r}_{a\, l_a\, l'_a} = \mathbf{r}_a + l_a\, \mathbf{e} + l'_a\, \mathbf{e}' \ , \quad \text{for} \quad a = 1, 2 \ , \tag{30}$$

where l_a and l'_a are integer, and $\mathbf{r}_a$ is the position vector of the disk a with respect to the center of the cell. Therefore, the distance between the two disks is expressed by

$$\| \, \mathbf{r}_{1\, l_1\, l'_1} - \mathbf{r}_{2\, l_2\, l'_2} \, \| = \| \, \underbrace{\mathbf{r}_1 - \mathbf{r}_2}_{\mathbf{r}} + (l_1 - l_2)\, \mathbf{e} + (l'_1 - l'_2)\, \mathbf{e}' \, \| \ , \tag{31}$$

where $\mathbf{r} = \mathbf{r}_1 - \mathbf{r}_2$ is the relative position between both disks. By the minimum image convention, the relative distance $\|\mathbf{r}\|$ should take the smallest value among the infinitely many possible values. Of course, this distance has to be greater than or equal to the disk diameter ($\|\mathbf{r}\| = \|\mathbf{r}_1 - \mathbf{r}_2\| \geq \sigma$). As we have a hard-disk potential, the disks move in a free motion between each collision. Therefore, the equations of motion are written as:

$$\begin{cases} \dfrac{d\mathbf{r}_1}{dt} = \dfrac{\mathbf{p}_1}{m} + \displaystyle\sum_s \Delta\mathbf{r}_1^{(s)}\ \delta(t - t_s) \ , \\ \dfrac{d\mathbf{r}_2}{dt} = \dfrac{\mathbf{p}_2}{m} + \displaystyle\sum_s \Delta\mathbf{r}_2^{(s)}\ \delta(t - t_s) \ , \end{cases} \tag{32}$$

$$\begin{cases} \dfrac{d\mathbf{p}_1}{dt} = \mathbf{F}_1 \ , \\ \dfrac{d\mathbf{p}_2}{dt} = \mathbf{F}_2 \ , \end{cases} \tag{33}$$

where $\mathbf{p}_1$ and $\mathbf{p}_2$ are the momenta of the two disks, $\mathbf{F}_1$ and $\mathbf{F}_2$ being the forces applied respectively to the disks 1 and 2. These forces equal zero when $\|\mathbf{r}_1 - \mathbf{r}_2\| > \sigma$ and are infinitely repulsive when $\|\mathbf{r}_1 - \mathbf{r}_2\| = \sigma$. t_s denotes the time of the jump to satisfy the minimum image convention.

At this stage, we can do the following change of variables:

$$\begin{cases} \mathbf{r} = \mathbf{r}_1 - \mathbf{r}_2 \ , \\ \mathbf{R} = \dfrac{\mathbf{r}_1 + \mathbf{r}_2}{2} \ , \end{cases} \tag{34}$$

$$\begin{cases} \mathbf{p} = \dfrac{\mathbf{p}_1 - \mathbf{p}_2}{2} \ , \\ \mathbf{P} = \mathbf{p}_1 + \mathbf{p}_2 \ . \end{cases} \tag{35}$$

If we introduce the reduced mass $\mu = \frac{m}{2}$, we can write:

$$\mu \, \frac{d\mathbf{r}}{dt} \;=\; \mathbf{p} + \sum_s \mu \, \Delta\mathbf{r}^{(s)} \, \delta(t - t_s) = \mu \, \mathbf{v} + \sum_s \mu \, \Delta\mathbf{r}^{(s)} \, \delta(t - t_s) \; , \tag{36}$$

$$\frac{d\mathbf{p}}{dt} \;=\; \mathbf{F} = \mathbf{F}_1 = -\mathbf{F}_2 \; , \tag{37}$$

where $\mathbf{v}$ is the relative velocity and $\Delta\mathbf{r}^{(s)} = \Delta\mathbf{r}_1^{(s)} - \Delta\mathbf{r}_2^{(s)}$. Here we suppose that we are in the reference frame of the mass center (that is $\mathbf{P} = 0$). Accordingly, the energy of the system is reduced to:

$$E = \frac{\mathbf{p}^2}{2\,\mu} \; . \tag{38}$$

The interest of this change of variables is to reduce the number of variables. Indeed, the only variables that remain are the relative position and velocity [$\mathbf{r} = (x, y)$ and $\mathbf{v} = (v_x, v_y)$]. We can associate a fictitious pointlike particle with these variables, which moves in a reduced system, known as the *periodic Sinai billiard* (see Fig. 3).

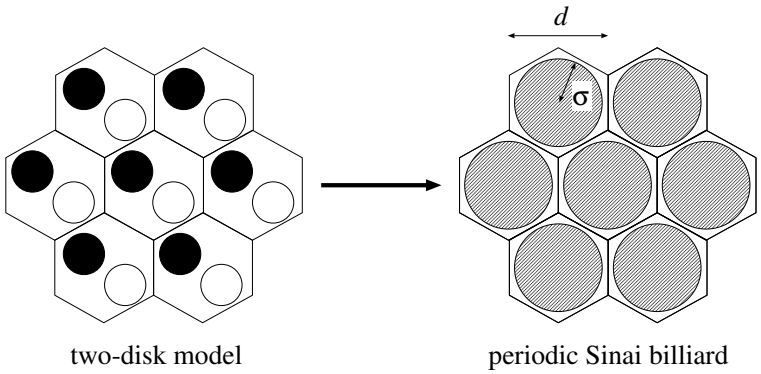

FIG. 3: The model of two hard disks in the hexagonal geometry is reduced to the periodic Sinai billiard thanks to a change of variables.

The billiard is also a triangular lattice of hexagonal cells. The size d of these cells is equal to the size of the cells of the model itself ($d = L$). A hard disk is fixed on the center of each cell. Its radius is equal to the diameter σ of the two moving disks.

The basis vectors of this lattice are the same as those of the original dynamics (32)-(33) if we replace L by d, which gives us the possibility to spot a cell in the lattice thanks to the vector:

$$\mathbf{r}_c = l_c \, \mathbf{e} + l'_c \, \mathbf{e}' \; , \tag{39}$$

where l_c and l'_c are integer.

In the Sinai billiard, the system is described by a trajectory in a four-dimensional phase space which are the Cartesian coordinates (x, y, p_x, p_y), or the polar coordinates (x, y, p_θ, θ). However, since the energy of the system is conserved, this space is reduced to the three-dimensional space of the variables (x, y, θ). Furthermore, in hard-ball systems, the topology of the trajectory is independent of the energy level. Therefore, we can study the system on an arbitrary energy level. This energy determines the temperature of the system and is equal to $E = (d/2)(N-1)k_{\rm B}T = k_{\rm B}T$ because we have only two degrees of freedom ($d = 2$, $N = 2$). Sinai and Bunimovich have demonstrated that the dynamics in such billiards is ergodic on each energy level [15, 16].

B. Square geometry

The case of the square geometry is similar to the hexagonal one except that the basis vectors are here given by

$$\begin{cases} \mathbf{e} = (L, 0) \; , \\ \mathbf{e}' = (0, L) \; , \end{cases} \tag{40}$$

where L is the length of a side of the square unit cell which contains two moving disks of diameter σ. We perform the same change of variables to reduce the dynamics of two hard disks to the one of the fictitious pointlike particle of a Sinai billiard in a square unit cell. Here also, the size d of the cells of the Sinai billiard is the same as for the cells of the two hard disks model: $d = L$.

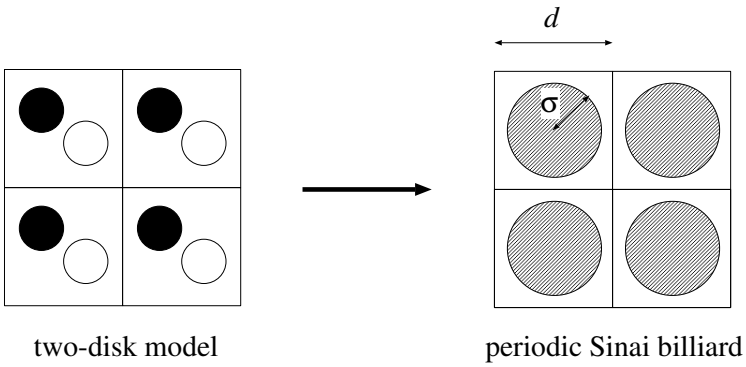

FIG. 4: The model of two hard disks in the square geometry is reduced to the periodic Sinai billiard thanks to a change of variables.

C. The different dynamical regimes of the model

The physical quantity determining the size of the cell in our model is the density which corresponds to the number of disks per unit volume or, in our case, the number of disks per unit area. Each cell contains two disks. Therefore, the density is $n = \frac{2}{V}$ where $V = \|\mathbf{e} \times \mathbf{e}'\|$ is the area of a cell. In our study, we have chosen that the diameter of the moving disks is equal to the unity: $\sigma = 1$.

As a function of the density, we observe different dynamical regimes. At low density, the disks are able to move in the whole lattice so that the disks are not localized in bounded phase-space regions. In this case, the billiard may have a finite or an infinite horizon depending on the geometry and on the density. In the opposite, at high density, the disks are so close to each other that they cannot travel across the system and we refer to this regime as the *localized regime*. The critical density between the nonlocalized and localized regimes corresponds to the situation where both disks have a double contact with each other in the configuration shown in Fig. 5.

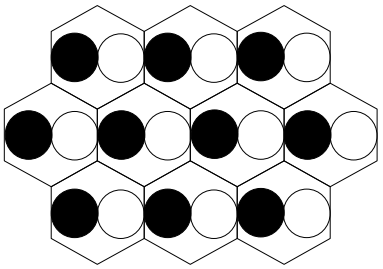

FIG. 5: Hexagonal system at the critical density $n_{\rm cr}$.

1. *Hexagonal geometry*

In the hexagonal geometry, the area of the system is $V = \|\mathbf{e} \times \mathbf{e}'\| = \frac{\sqrt{3}}{2} L^2$ and the critical density is equal to:

$$n_{\rm cr} = \frac{\sqrt{3}}{3} \simeq 0.5774 \,, \tag{41}$$

even though the maximum density (the *close-packing density*) is:

$$n_{\max} = \frac{4\sqrt{3}}{9} \simeq 0.7698 \, . \tag{42}$$

At the close-packing density, the system forms a triangular crystal.

In the Sinai billiard, it is well known that there exists different kinds of regimes according to the dynamics of the particles. As a function of the density n, we observe three regimes:

- **The infinite-horizon regime:** At the low densities $0 < n < \frac{\sqrt{3}}{4}$, the particles can move in free flight over arbitrarily large distances. In this regime, the self-diffusion coefficient is infinite. (See Fig. 6.)

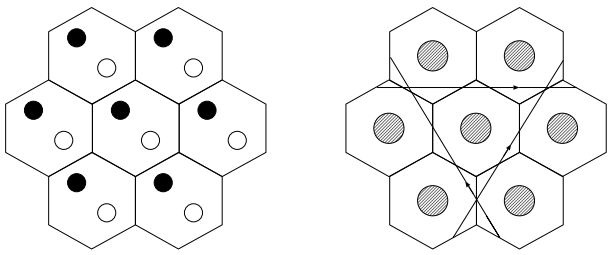

FIG. 6: Typical configuration of the system in the infinite-horizon regime.

- **The finite-horizon regime:** For the intermediate densities $\frac{\sqrt{3}}{4} < n < n_{\rm cr}$, the free flights between the collisions are always bounded by a finite distance of the order of the interdisk distance d. Therefore, the horizon is finite and the self-diffusion coefficient is positive and finite. (See Fig. 7.)

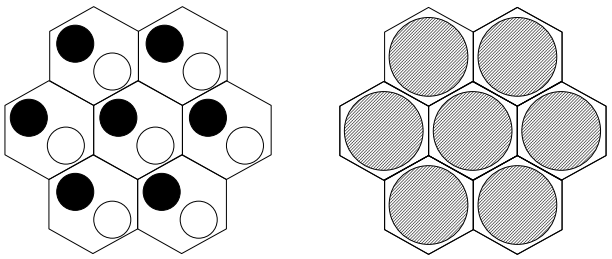

FIG. 7: Typical configuration of the system in the finite-horizon regime.

- **The localized regime:** At the highest densities $n_{\rm cr} < n < n_{\max}$, the images of the disk overlap each other in the billiard so that the relative motion of the particles is localized in bounded regions. Therefore, the self-diffusion coefficient vanishes. (See Fig. 8.)

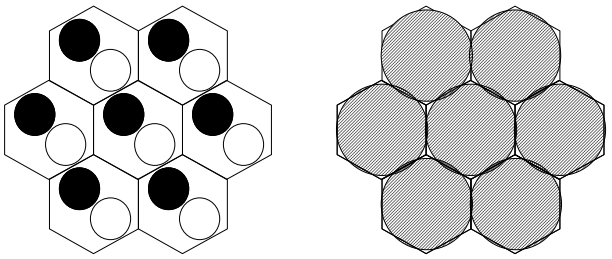

FIG. 8: Typical configuration of the system in the localized regime.

We notice that Figs. 6, 7 and 8 are not depicted at the same scale since the disk diameter is fixed to unity ($\sigma = 1$) and it is the interdisk distance d that varies.

The infinite- and finite-horizon regimes extend over the densities $0 < n < n_{\rm cr}$. The localized regime corresponds to the densities $n_{\rm cr} < n < n_{\rm max}$. The following figure 9 shows the different regimes in the hexagonal geometry. The remarkable feature of the hexagonal geometry is that there exists a finite-horizon regime which is not localized, in contrast to the square geometry (see below).

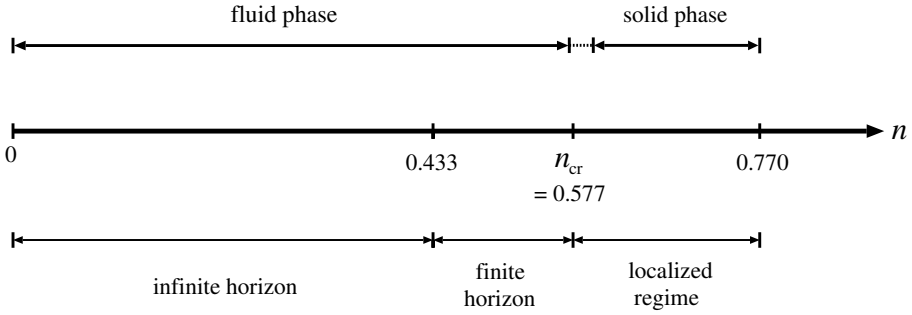

FIG. 9: The different dynamical regimes and thermodynamic phases of the model in the hexagonal geometry versus the density n.

2. *Square geometry*

In the square geometry, the volume is $V = \|\mathbf{e} \times \mathbf{e}'\| = L^2$ and the critical density is:

$$n_{\rm cr} = 0.5 \ , \tag{43}$$

which is the density of the transition between the infinite-horizon and the localized regimes. The close-packing density is equal to:

$$n_{\rm max} = 1 \ . \tag{44}$$

In Fig. 10, we have depicted the different regimes in the square geometry. In the square geometry, there also exist nonlocalized and localized regimes, but the horizon is always infinite in the nonlocalized regime. Therefore, it is only in the localized regime that the horizon is finite in the square geometry. This is an important difference with respect to the hexagonal geometry.

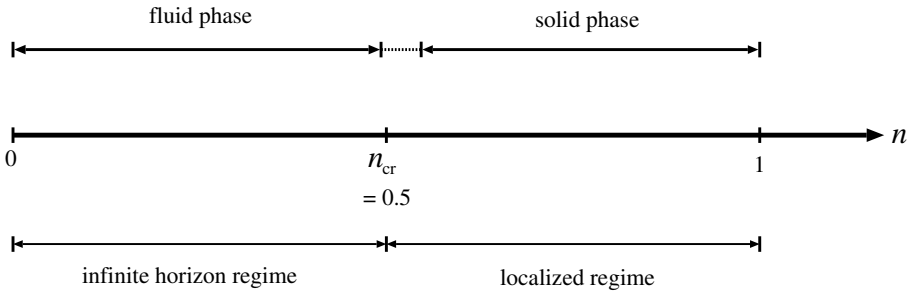

FIG. 10: The different dynamical regimes and thermodynamic phases of the model in the square geometry versus the density n.

IV. PROPERTIES OF THE MODEL

A. Mean free path

The *mean free path* $\langle l \rangle$ is the average distance between two successive collisions. It is known that, in two-dimensional billiards, the mean free path is related to the area $\mathcal{A}$ of the billiard and its perimeter $\mathcal{L}$ according to [17]

$$\langle l \rangle = \frac{\pi \mathcal{A}}{\mathcal{L}} \ . \tag{45}$$

In the different regimes, the mean free path is given by

- hexagonal geometry:

  (i) $\langle l \rangle = \frac{1}{n} - \frac{\pi}{2}$, $\qquad n \leq n_{\rm cr}$,

  (ii) $\langle l \rangle = \pi \frac{\frac{2}{n} - \pi + 6 \arccos(\frac{1}{\sqrt{\sqrt{3}\, n}}) - \frac{6}{\sqrt{\sqrt{3}\, n}} \sqrt{1 - \frac{1}{\sqrt{3}\, n}}}{2\pi - 12 \arccos(\frac{1}{\sqrt{\sqrt{3}\, n}})}$, $\qquad n \geq n_{\rm cr}$;

- square geometry:

  (i) $\langle l \rangle = \frac{1}{n} - \frac{\pi}{2}$, $\qquad n \leq n_{\rm cr}$,

  (ii) $\langle l \rangle = \pi \frac{\frac{2}{n} - \pi + 4 \arccos(\frac{1}{\sqrt{2\, n}}) - 2\sqrt{\frac{2}{n}} \sqrt{1 - \frac{1}{2\, n}}}{2\, \pi - 8 \arccos(\frac{1}{\sqrt{2\, n}})}$, $\qquad n \geq n_{\rm cr}$.

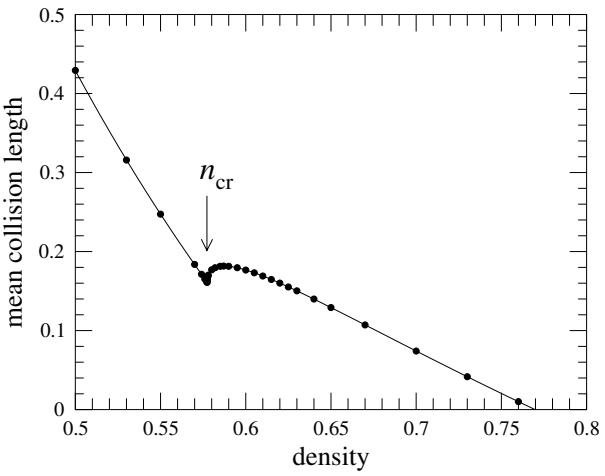

FIG. 11: Theoretical (continuous line) and numerical (dots) values of the mean free path versus the density n in the hexagonal geometry.

We show in Figs. 11 and 12 the excellent agreement between the above expressions and the values obtained by numerical simulations. The break observed in Figs. 11 and 12 between the nonlocalized and localized regimes can be explained thanks to Eq. (45). Indeed, at the critical density $n_{\rm cr}$, the disks form a horn. Above criticality, the horn becomes a corner with a finite angle so that the perimeter $\mathcal{L}$ decreases very fast. But, on the other hand, the area $\mathcal{A}$ remains relatively constant. Therefore the ratio $\frac{\mathcal{A}}{\mathcal{L}}$ increases with n until this effect disappears. At higher densities, the mean free path decreases again.

B. Pressure and the different phases of the model

The hydrostatic pressure allows us to interpret the different regimes in terms of thermodynamic phases. The pressure can be calculated in terms of the time average of the Helfand moment as shown in Appendix C. In the

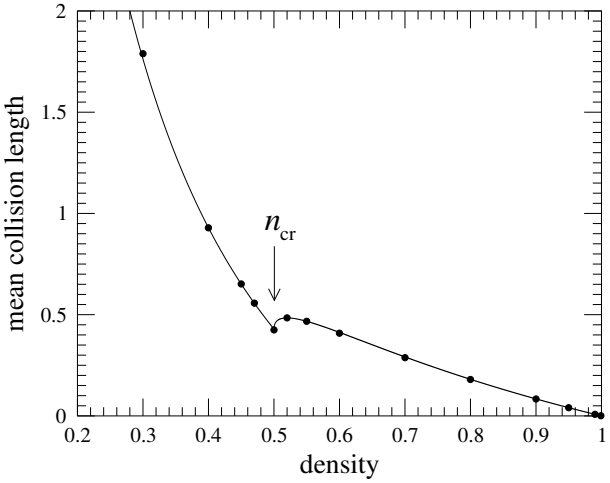

FIG. 12: Theoretical (continuous line) and numerical (dots) values of the mean free path versus the density n in the square geometry.

two-disk model with $N = 2$ and $d = 2$, the pressure is given by

$$PV = k_{\rm B}T + R \, , \tag{46}$$

where the rest can be calculated according to Eq. (C8) as

$$R = \frac{\langle \Delta \mathbf{p}_1^{(c)} \cdot \mathbf{r}_{12}^{(c)} \rangle}{4 \, \langle \Delta t_{c-1,c} \rangle} \, , \tag{47}$$

where $\langle \Delta t_{c-1,c} \rangle$ is the mean intercollisional time. If we denote by $\phi^{(c)}$ the angle between the velocity at collision and the normal to the disk of the Sinai billiard, the average in the numerator becomes

$$\langle \Delta \mathbf{p}_1^{(c)} \cdot \mathbf{r}_{12}^{(c)} \rangle = m \, v \, \sigma \, \langle \cos \phi^{(c)} \rangle \, , \tag{48}$$

σ being the diameter of the disks. In the case the total momentum vanishes, the velocity $\mathbf{v}$ of the trajectory in the billiard is related to the relative momentum $\mathbf{p}$, the energy, and the temperature by

$$E = k_{\rm B}T = \frac{\mathbf{p}^2}{2\mu} = \frac{\mathbf{p}^2}{m} = \frac{\mu \mathbf{v}^2}{2} = \frac{m \mathbf{v}^2}{4} \, , \tag{49}$$

so that $\mathbf{v} = 2\mathbf{p}/m$. At collision, $\sin \phi^{(c)}$ is uniformly distributed in the interval $[-1, +1]$ so that

$$\langle \cos \phi^{(c)} \rangle = \frac{\pi}{4} \, . \tag{50}$$

On the other hand, the mean intercollisional time of the billiard is related to the mean free path $\langle l \rangle$ and the speed $v = \|\mathbf{v}\|$ by

$$\langle \Delta t_{c-1,c} \rangle = \frac{\langle l \rangle}{v} \, . \tag{51}$$

Gathering the results, we obtain the rest as

$$R = \frac{\pi \, \sigma \, m \, v^2}{16 \, \langle l \rangle} = \frac{\pi \, \sigma}{4 \, \langle l \rangle} \, k_{\rm B}T \, . \tag{52}$$

Accordingly, the hydrostatic pressure of the model is given by

$$PV = k_{\rm B}T \left(1 + \frac{\pi \sigma}{4 \langle l \rangle} \right) = k_{\rm B}T \left(1 + \frac{\sigma \mathcal{L}}{4 \mathcal{A}} \right) \, . \tag{53}$$

In our work, we introduce the reduced pressure defined as

$$P^* \equiv \beta P \frac{V}{N} = \frac{PV}{(N-1)k_{\rm B}T} = 1 + \frac{\pi\sigma}{4\langle l\rangle} = 1 + \frac{\sigma\mathcal{L}}{4\mathcal{A}} \; . \tag{54}$$

In Figs. 13 and 14, the reduced pressure is depicted as a function of the density and we observe the manifestation of a phase transition around the critical density. The hard-ball systems are known to present a fluid-solid phase transition that we here already observe in the two-disk model.

At low density, the fictitious particle of the Sinai billiard can diffuse in the whole lattice. This means that the two disks move over arbitrarily large distances one with respect to the other, which is a feature of a fluid phase. In contrast, at high density, the fictitious particle is trapped between three (or four) disks and its motion is reminiscent of the vibration of atoms in a solid. Of course, it is not really a vibration since the disks bounce in a chaotic motion because of the elastic collisions whereas, in a solid, the atoms have quasi-harmonic oscillations around their equilibrium position. Nevertheless, we are in the presence of a solid phase because the translational invariance is broken. Indeed, the motion is no longer ergodic because the motion now is confined into one among several phase-space domains of the energy shell.

A phase transition occurs between the fluid and solid phases. At the critical density $n_{\rm cr}$, the pressure has a maximum. Above $n_{\rm cr}$, the pressure decreases, reaches a minimum at a value $n'_{\rm cr} > n_{\rm cr}$, before increasing again. For $n_{\rm cr} < n < n'_{\rm cr}$, the compressibility would be negative so that this state would be unstable from a thermodynamic viewpoint. This suggests a Maxwell construction to determine a fluid-solid coexistence in the interval of densities $n_{\rm F} < n < n_{\rm S}$ with $n_{\rm F} < n_{\rm cr}$ and $n'_{\rm cr} < n_{\rm S}$. The values which would delimit this small coexistence interval in a thermodynamic interpretation of the transition would be given by

$$\begin{aligned} \bullet \text{ hexagonal geometry:} \qquad n_{\rm F} &= 0.57 \pm 0.01 \; , \\ n_{\rm S} &= 0.60 \pm 0.01 \; , \end{aligned} \tag{55}$$

and

$$\begin{aligned} \bullet \text{ square geometry:} \qquad n_{\rm F} &= 0.49 \pm 0.01 \; , \\ n_{\rm S} &= 0.55 \pm 0.01 \; , \end{aligned} \tag{56}$$

(see Figs. 9 and 10). In the square geometry, the horizon is infinite in the fluid phase. In the hexagonal geometry, the horizon may also be finite in the fluid phase, which leads to finite viscosity coefficients in the fluid phase of this model as shown in the following.

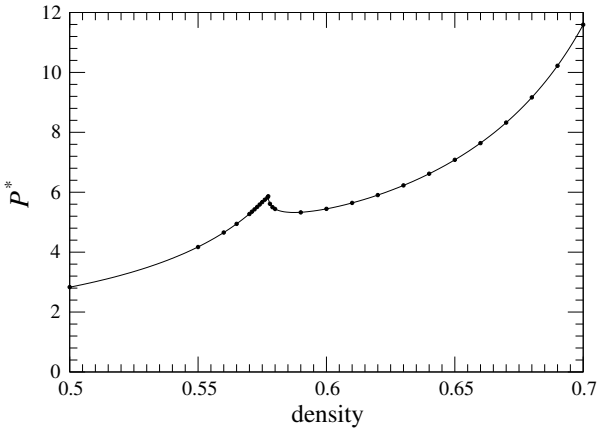

FIG. 13: Theoretical (continuous line) and numerical (dots) values of the reduced pressure P^* versus the density n in the hexagonal geometry.

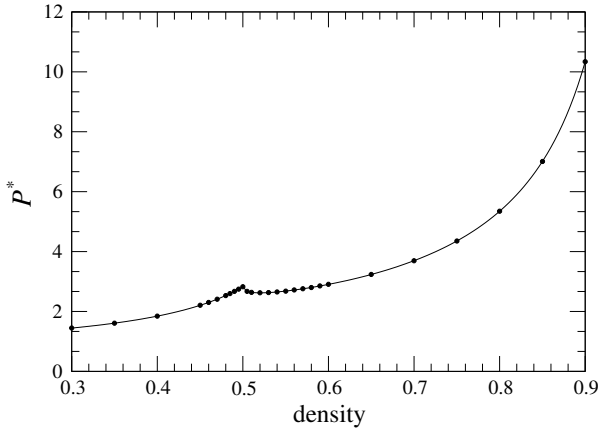

FIG. 14: Theoretical (continuous line) and numerical (dots) values of the reduced pressure P^* versus the density n in the square geometry.

V. VISCOSITY IN THE TWO-HARD-DISK MODEL

A. The Helfand moment in the two-hard-disk model

In our model defined with Eqs. (34) and (35) and with a vanishing total momentum $\mathbf{P} = \mathbf{0}$, the forces obey $\mathbf{F}_1 = -\mathbf{F}_2 = \mathbf{F}$ and the microscopic current can be written in relative coordinates as

$$J_{ij} = 2\,\frac{p_i p_j}{m} + F_i\, r_j\ , \tag{57}$$

where $\mathbf{r}$ is the smallest distance between the disks 1 and 2. Following the minimum image convention the position vector presents discontinuities because of the passages of the relative position through a boundary, after which it is reinjected into the cell at the opposite boundary. We denote the vectors normal to the boundaries of the unit cell by

$$\text{hexagonal geometry}: \begin{cases} \mathbf{c}_1 = \mathbf{a}\ , \\ \mathbf{c}_2 = -\mathbf{a}\ , \\ \mathbf{c}_3 = \mathbf{b}\ , \\ \mathbf{c}_4 = -\mathbf{b}\ , \\ \mathbf{c}_5 = \mathbf{b} - \mathbf{a}\ , \\ \mathbf{c}_6 = \mathbf{a} - \mathbf{b}\ , \end{cases} \tag{58}$$

and

$$\text{square geometry}: \begin{cases} \mathbf{c}_1 = \mathbf{a}\ , \\ \mathbf{c}_2 = -\mathbf{a}\ , \\ \mathbf{c}_3 = \mathbf{b}\ , \\ \mathbf{c}_4 = -\mathbf{b}\ . \end{cases} \tag{59}$$

In order to satisfy the minimum image convention, the relative position undergoes jumps by vectors which are the vectors normal to the unit cell so that $\Delta\mathbf{r}^{(s)} = -\mathbf{c}_{\omega_s}$ where ω_s denotes the label of the boundary crossed by the particle at the s^{th} passage at time t_s. In these notations, Hamilton's equations take the form

$$\begin{cases} \frac{d\mathbf{r}}{dt} = \frac{2\mathbf{p}}{m} - \sum_s \mathbf{c}_{\omega_s}\,\delta(t - t_s)\ , \\ \frac{d\mathbf{p}}{dt} = \mathbf{F}\ . \end{cases} \tag{60}$$

In this periodic system, the expression for the Helfand moment is given by a reasoning similar to the one leading to Eq. (16). We obtain:

$$G_{ij}(t) = p_i(t)\, r_j(t) + \sum_s p_i(t_s)\, c_{\omega_s j}\, \theta(t - t_s)\ . \tag{61}$$

Finally, the viscosity coefficients have the expressions:

$$\eta_{ij,kl} = \lim_{t\to\infty} \frac{\beta}{2tV} \left(\left\langle \sum_{t_s<t} p_i(t_s)\, c_{\omega_s j} \sum_{t_{s'}<t} p_k(t_{s'})\, c_{\omega_{s'} l} \right\rangle - \left\langle \sum_{t_s<t} p_i(t_s)\, c_{\omega_s j} \right\rangle \left\langle \sum_{t_{s'}<t} p_k(t_{s'})\, c_{\omega_{s'} l} \right\rangle \right) . \tag{62}$$

Let us remark that the terms $p_i(t)\, r_j(t)$ do not appear in this relation because they do not contribute to the viscosity coefficients. Indeed, the relative position $\mathbf{r}(t)$ and momentum $\mathbf{p}(t)$ remain bounded in the course of time and their contribution disappears in the limit $t \to \infty$.

In the following, the numerical results are presented in terms of a reduced viscosity tensor which is defined by

$$\eta^*_{ij,kl} \equiv \frac{\eta_{ij,kl}}{2\sqrt{m k_{\rm B} T}} . \tag{63}$$

B. Hexagonal geometry

In the hexagonal geometry the fourth-order tensor of viscosity is isotropic. Indeed, since the system is invariant under rotations by $\frac{\pi}{3}$, we obtain the relation $\eta_{xx,yy} = \eta_{xx,xx} - 2\, \eta_{xy,xy}$ which implies the full rotation invariance of the viscosity tensor. We depict in Figs. 15 and 16 the results obtained for the reduced viscosities (η^*, ζ^*) and the relation (28) is checked in Fig. 17.

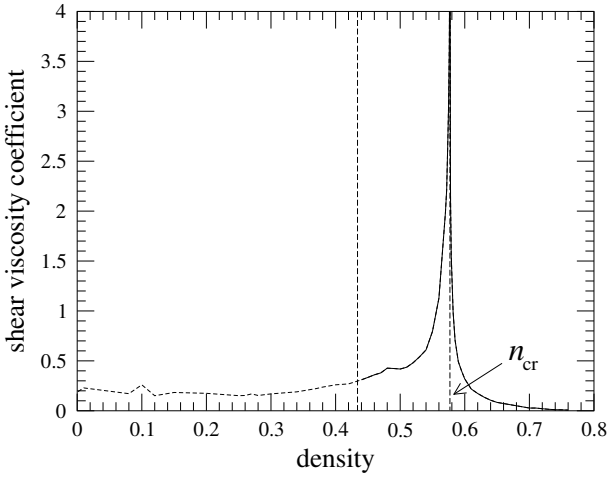

FIG. 15: Shear viscosity coefficient η^* versus the density in the hexagonal geometry. The part in dashed line corresponds to the density in which the coefficient would not exist in the limit $t \to \infty$ because the horizon is infinite. The long dashed vertical lines separate the different regimes: on the left-hand side, the horizon-infinite regime (fluid phase); at the center, the horizon-finite regime (fluid phase); and on the right-hand side, localized regime (solid phase).

In the infinite-horizon regime, the trajectory can present arbitrarily large displacements in the system without undergoing any collision. Accordingly, the variance of the Helfand moment G_{yx} increases faster than linearly as $t\, \log t$, which implies an infinite viscosity coefficient after averaging over an infinite time interval. However, the factor $\log t$ generates a so weak growth that it does not manifest itself much over the finite time of the simulation. This is the reason why we obtain finite values for the viscosity coefficients in Figs. 15 and 16. However, these values are only indicative since they should be infinite, strictly speaking.

On the other hand, in the finite-horizon regime, the variance of the Helfand moment has a strictly linear increase in time and the viscosity coefficients are finite and positive. This is the result of a central-limit theorem which holds in the finite-horizon regime of the hexagonal geometry, as can be proved by considerations similar to those developed by Bunimovich and Spohn [10]. We observe in Fig. 15 that the viscosity has a diverging singularity at the critical density ($n_{\rm cr} = \frac{\sqrt{3}}{3}$) which corresponds to the fluid-solid phase transition. We shall explain below the origin of this singularity.

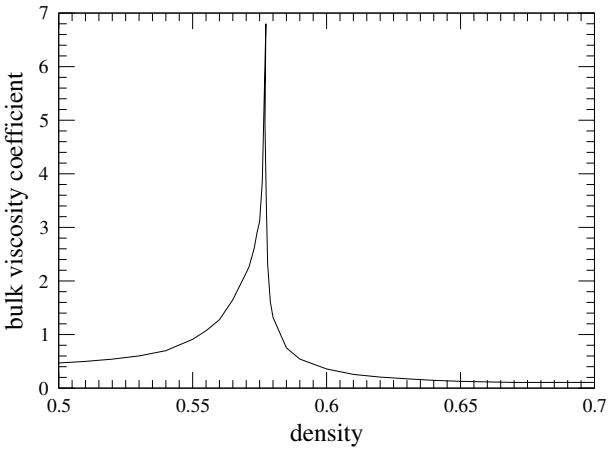

FIG. 16: Bulk viscosity coefficient ζ^* versus the density in the hexagonal geometry.

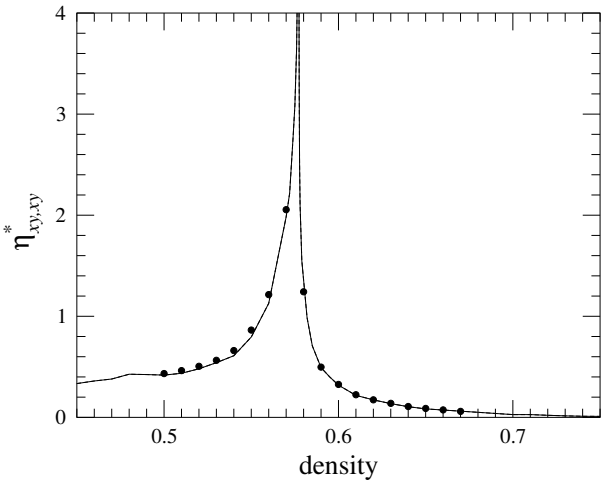

FIG. 17: Tensor element $\eta^*_{xy,xy}$ of shear viscosity versus the density in the hexagonal geometry. The dots represent the results of the relation (28): $\eta^*_{xy,xy} = \frac{1}{2}\left(\eta^*_{xx,xx} - \eta^*_{xx,yy}\right)$. The continuous line corresponds to the data of Fig. 15.

Finally, in the localized regime corresponding to the solid phase, the viscosity is finite and positive, and decreases when the density increases until the maximum density.

C. Square geometry

In the square geometry, the fourth-order viscosity tensor is not isotropic. Indeed, the tensor is transformed by the matrix $R_{ij}(\varphi)$ of rotation by an angle φ into

$$\eta_{ij,kl}(\varphi) = R_{ii'}(\varphi)\, R_{jj'}(\varphi)\, R_{kk'}(\varphi)\, R_{ll'}(\varphi)\, \eta_{i'j',k'l'}(0)\ . \tag{64}$$

For example, if $\varphi = \frac{\pi}{4}$, we have:

$$\begin{cases} \eta_{xx,xx}(\frac{\pi}{4}) = \frac{1}{2}\left[\eta_{xx,xx}(0) + \eta_{xx,yy}(0) + 2\,\eta_{xy,xy}(0)\right]\ , \\ \eta_{xy,xy}(\frac{\pi}{4}) = \frac{1}{2}\left[\eta_{xx,xx}(0) - \eta_{xx,yy}(0)\right]\ , \\ \eta_{xx,yy}(\frac{\pi}{4}) = \frac{1}{2}\left[\eta_{xx,xx}(0) + \eta_{xx,yy}(0)\right] - \eta_{xy,xy}(0)\ . \end{cases} \tag{65}$$

Since the system is not isotropic, one more viscosity coefficient is required beside the shear and bulk viscosities. Therefore, we have to evaluate the three independent tensor elements $\eta_{xx,xx}, \eta_{xy,xy}, \eta_{xx,yy}$ which are depicted in Figs. 18 and 19 with respect to two different axis frames: in the first one the axes are parallel to the sides of the square ($\varphi = 0$) and, in the second one, they form an angle of 45 degrees with respect to the lattice ($\varphi = \frac{\pi}{4}$). Figure 19 shows that the relations (65) are well satisfied between the elements of the viscosity tensor.

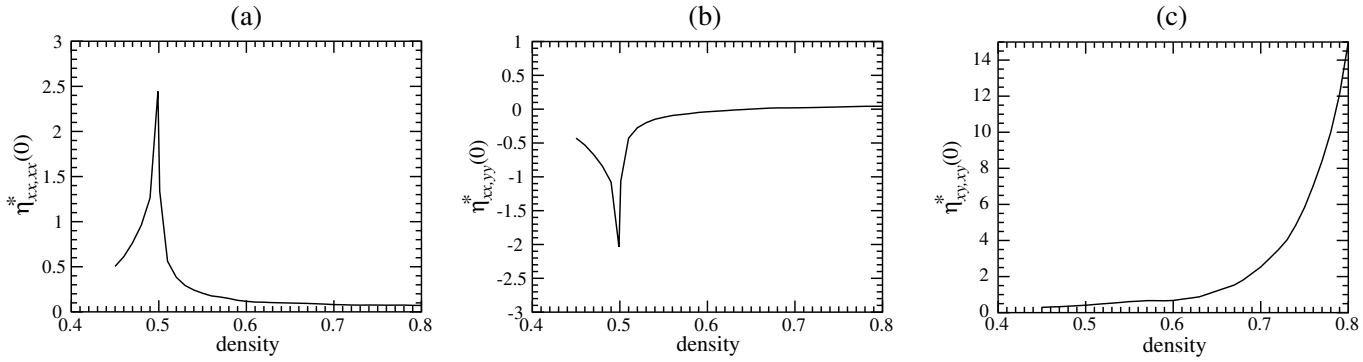

FIG. 18: Square geometry: The three independent tensor elements (a) $\eta^*_{xx,xx}$, (b) $\eta^*_{xx,yy}$, (c) $\eta^*_{xy,xy}$ for $\varphi = 0$.

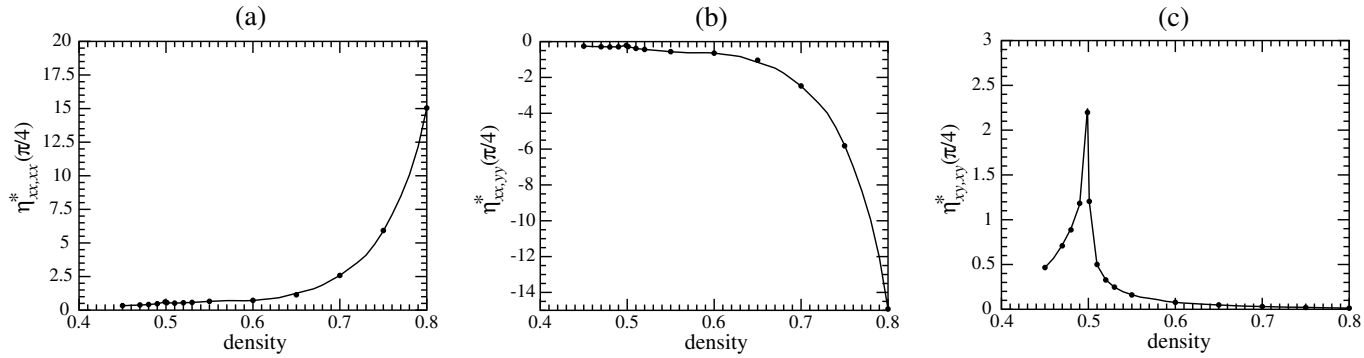

FIG. 19: Square geometry: The three independent tensor elements (a) $\eta^*_{xx,xx}$, (b) $\eta^*_{xx,yy}$, (c) $\eta^*_{xy,xy}$ for $\varphi = \frac{\pi}{4}$. The continuous line corresponds to the results obtained numerically and the dots to the values obtained by the relations (65).

In the square geometry, Bunimovich and Spohn have proved a central-limit theorem for viscosity in the localized regime which coincides with the solid phase above the critical density [10]. In this range of density, the viscosity coefficient is thus guaranteed to be positive and finite.

In the fluid phase, the horizon is infinite and the viscosity is infinite because of a growth as $t \log t$ of the variance of the Helfand moment for a reason similar as in the hexagonal geometry. In our numerical simulation over a finite time interval, the viscosity takes finite values because the logarithmic growth is very slow.

An important difference with respect to the hexagonal geometry is the absence of a singularity of the viscosity coefficient $\eta^*_{xy,xy}(0)$ at the phase transition in the square geometry. However, such a singularity still appears in the square geometry in the coefficients $\eta^*_{xx,xx}(0)$, $\eta^*_{xx,yy}(0)$, and $\eta^*_{xy,xy}(\frac{\pi}{4})$.

Moreover, in the solid phase, the coefficient $\eta^*_{xy,xy}(0)$ increases with the density, as explained here below.

D. Explanation of the numerical observations

1. *Solid phase*

The behavior of the viscosity tensor is clearly different in the two geometries. In this section, we explain these differences by comparing the topology of the trajectories in both geometries, since these trajectories form the basis of

the evolution of the Helfand moment. More precisely, we will compare the behavior of $\eta^*_{xy,xy}$ between the hexagonal and square geometries for $\varphi = 0$. This viscosity coefficient is given by

$$\begin{cases} \eta^*_{xy,xy} = \eta^*_{yx,yx} \sim \frac{\langle G_{yx}(t)^2 \rangle}{t} \ , \\ G_{yx} \sim \sum_s v_y(t_s)\, c_{\omega_s x} \ , \end{cases} \qquad \langle G_{yx}(t) \rangle = 0 \ , \tag{66}$$

where $v_y(t_s)$ is the y-component of the velocity at the time t_s of the jump.

When the density tends to the closed-packing density, the accessible domain of the particles tends to a perfect triangle in the hexagonal geometry. On the other hand, in the square geometry, it tends to a perfect square. This difference is at the origin of the different behaviors of the $\eta^*_{xy,xy}$ in both lattices.

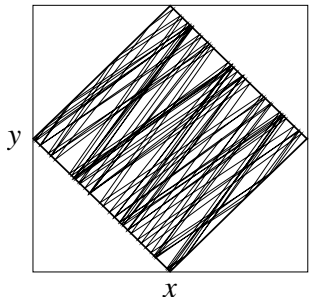

FIG. 20: Part of a typical trajectory in the square geometry when the density tends to the closed-packing density.

First, let us consider the case of the square geometry. In Fig. 20, we depict a typical trajectory of the fictitious particle moving in the Sinai billiard. We observe that this trajectory presents a regular motion between two opposite "walls" (these walls are made of parts of the fixed hard disks in the billiard). At the limit where the billiard is a perfect square, the trajectories will bounce back and forth in a regular motion. Indeed the square billiard is an *integrable system*.

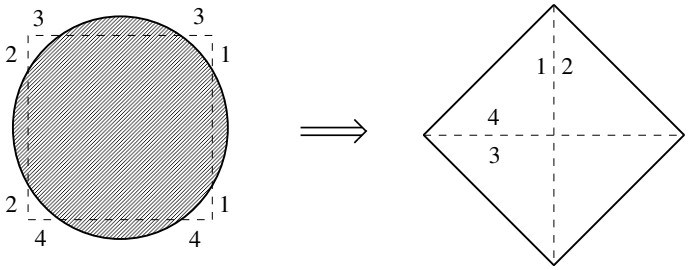

FIG. 21: Geometry and notation for the boundaries in the case of the square geometry at high density.

As we have seen before, the evolution of the Helfand moment along the trajectories is determined by the passages through the boundaries (see Fig. 21). Both horizontal boundaries (3 and 4) do not contribute to the evolution of G_{yx} since the x-component of the normal vectors to these boundaries equals zero. Therefore, only the passages through the vertical boundaries contribute to the Helfand moment in the square geometry.

To understand the behavior of the Helfand moment, let us take a small part of the typical trajectory drawn in Fig. 20 (see Fig. 22). First, let us consider the part denoted by the letter a in Fig. 22. This one crosses the boundary in the direction $1 \to 2$, which means that $c_{\omega_s x}$ is positive (since $c_{1x} = \frac{d}{2}$). On the other hand, the y-component of the velocity, v_y, is also positive. Therefore, the contribution of the small part a to the evolution of G_{yx} is positive.

Now, let us take the part of the trajectory denoted b in Fig. 22. In this case, the particle crosses the boundary in the direction $2 \to 1$ and c_{2x} is negative. Since v_y is also negative, the product of these two quantities is positive, and so at each successive crossings of the boundary $1 - 2$. Consequently, we obtain a sum of positive terms and the Helfand moment quickly increases along a trajectory as the one of Fig. 20.

However, the square is not perfect and the walls are still slightly convex. Therefore, after a certain time, the trajectory shown in Fig. 20 goes into a transient regime shown on the left-hand side of Fig. 23 before another regime in which the particle collides most often the two other walls (see the right-hand side of Fig. 23).

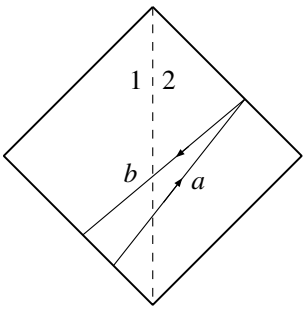

FIG. 22: Part of a typical trajectory in the square geometry at high density.

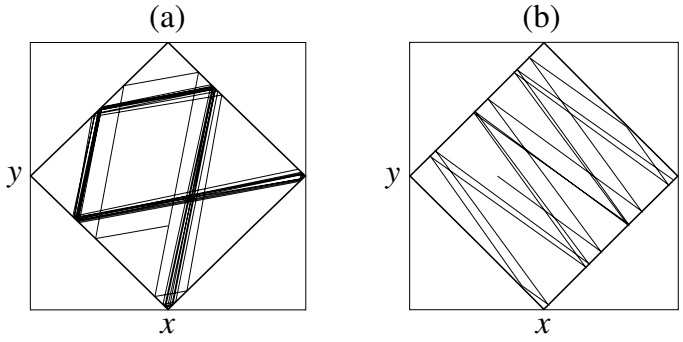

FIG. 23: Square geometry at high density: The trajectory is depicted (a) during a transient regime before (b) another regime with most bounces on the two other opposite walls.

With the same reasoning as before, we conclude that the contributions are negative in this new regime and the Helfand moment decreases during a long time interval.

The evolution of the Helfand moment along the whole trajectory is depicted in Fig. 24 where we observe the succession of the three types of regimes which we have described here above. We notice that the nearly constant part corresponds to the transient regime.

The larger is the density the more perfect is the square and the longer the trajectory remains in a particular regime. Therefore, the Helfand moment can have larger and larger variations, which implies an increase of the coefficient $\eta^*_{xy,xy}(0)$ of shear viscosity with density.

In the hexagonal geometry (see Fig. 25), the trajectories present another behavior. We show in Fig. 25 a typical trajectory in this geometry with a density larger than the critical density. We observe that the trajectory visits the whole billiard in different directions and therefore goes into very different velocities. Accordingly, the particle crosses the boundaries with random values of its velocity in contrast to its behavior in the square geometry. Consequently, the quantity $c_{\omega_s x}$ can be positive at a particular crossing and negative at the next one. Hence the Helfand moment cannot increase or decrease over long periods as in the square geometry (see Fig. 26). This explains qualitatively why, in the solid phase, the coefficient $\eta^*_{xy,xy}(0) = \eta^*$ is much smaller in the hexagonal geometry than in the square one.

In the square geometry with $\varphi = \frac{\pi}{4}$, the same arguments as in the hexagonal case explain the decrease of $\eta^*_{xy,xy}(\frac{\pi}{4})$ at high density. By the relations between the different elements of the viscosity tensor, we can also understand the behavior of the other elements in both geometries.

2. Fluid-solid phase transition

In both the hexagonal and square geometries, the two-disk model presents a phase transition. This transition is reminiscent of the fluid-solid phase transition in the many-disk system where the viscosity coefficient is also singular. In this regard, the two-disk model can contribute to the understanding of the changes in the transport properties

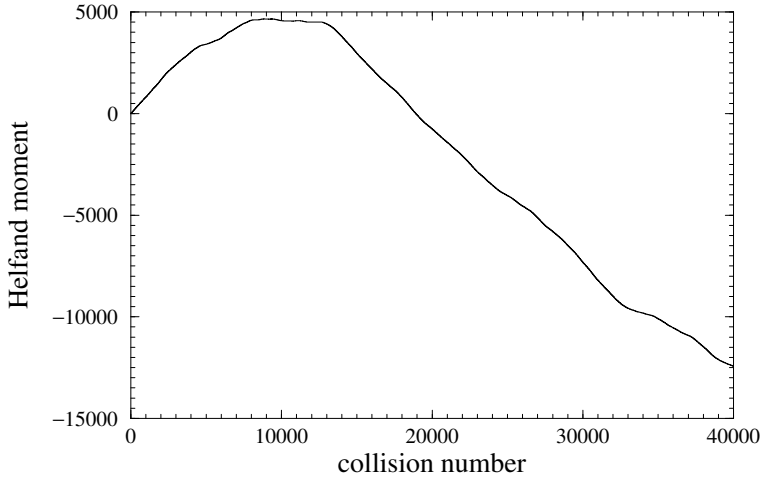

FIG. 24: Evolution of the Helfand moment along a typical trajectory in the square geometry at high density.

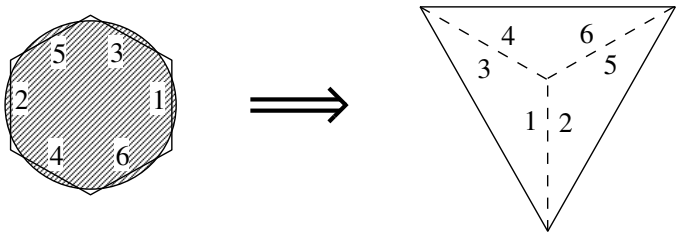

FIG. 25: Geometry and notation for the boundaries in the case of the hexagonal geometry at high density.

across the fluid-solid phase transition.

We first explain why $\eta^*_{xy,xy}$ presents a diverging singularity at the critical density in the hexagonal geometry and not in the square geometry for $\varphi = 0$. Here again, we compare the topology of the trajectories in both geometries and the way in which the Helfand moment evolves along these trajectories. At densities close to the critical density, both geometries present what we call *traps*.

Figure 27 shows an example of a trap. These traps are particular regions of the billiard where the particle can remain during a long time interval. Figure 28) depicts typical examples of a particle moving in such traps. When the particle travels out of the traps, the Helfand moment does not increase quickly in both geometries. Therefore, it is the presence of the traps which is at the origin of the difference between both geometries.

In the square geometry, the traps do not influence the evolution of G_{yx}. Indeed, as we have already mentioned here above, the passages through the horizontal boundary $3-4$ do not contribute since $c_{3x} = c_{4x} = 0$ (see Fig. 21 for the definitions of the boundaries in the square geometry). Therefore, the horizontal traps around these boundaries do not contribute. There remains the vertical traps. When a particle bounces for a long time in one of these traps, c_{1x} and c_{2x} are not vanishing, but the velocity v_y is almost equal to zero so that the vertical traps does not contribute much either. This implies that both kinds of traps contribute very slightly to the evolution of the Helfand moment. To conclude the Helfand moment diffuse in the same way as for the other densities and the coefficient $\eta^*_{xy,xy}(0)$ does not present any divergence at the fluid-solid transition in the square geometry.

On the other hand, in the hexagonal geometry, the traps along the boundaries making an angle of 30° with respect to the horizontal are very important for the evolution of G_{yx}, whereas the vertical traps do not participate significantly. Figure 29 shows a typical diffusion of the Helfand moment. We observe in Fig. 29 the presence of jumps which correspond to the passages in the traps like the one drawn on the left-hand side of Fig. 28. Because of these jumps, the Helfand moment quickly diffuses. Furthermore, the importance of these traps in the hexagonal geometry can also be understood by comparing the behavior of the Helfand moment as a function of time at densities below and above

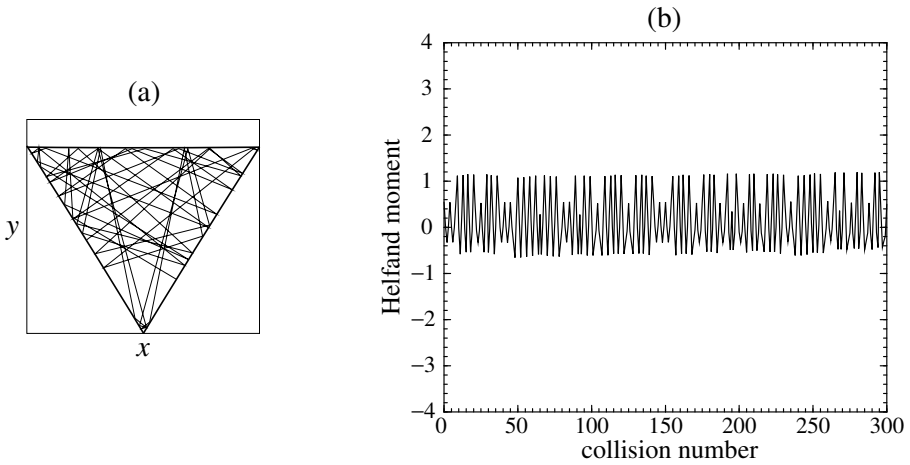

FIG. 26: Hexagonal geometry at high density: (a) Part of a typical trajectory when the density tends to the closed-packing density. (b) Evolution of the Helfand moment along this typical trajectory.

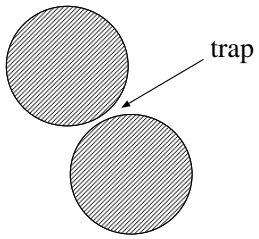

FIG. 27: Example of traps in which the particles can enter and remain a long time.

the critical one $n_{\rm cr}$.

We illustrate this point in Fig. 30 where we observe that there are no more jumps above the critical density. Therefore, G_{yx} does not vary much contrary to the case of densities just below $n_{\rm cr}$. Above criticality, the size of the traps decreases so quickly that the contribution of these traps decreases and, thus, the viscosity coefficient $\eta^*_{xy,xy} = \eta^*$ also decreases. By these arguments, we have an explanation for the diverging singularity of the shear viscosity at the phase transition in the hexagonal geometry.

This results show that, at a fluid-solid phase transition the viscosity coefficients may depend sensitively on the geometry of the lattice of the solid phase in formation.

E. Viscosity by the method of Alder *et al.*

We have also verified numerically that our method of calculation of the viscosity based on the Helfand moment (16) gives the same values as the method of Alder *et al.* based on the expression (21) [6]. In the two-disk system, this expression reduces to:

$$G_{ij}(t) = \sum_c \left[2\,\frac{p_i\,p_j}{m}\;\Delta t_{c-1,c} + \Delta p_i^{(c)}\; r_j(t_c)\;\theta(t-t_c) \right]. \tag{67}$$

As shown in Fig. 31 for the shear viscosity in the hexagonal geometry, there is an excellent agreement between the values obtained by both methods, which confirms the exact equivalence of both methods.

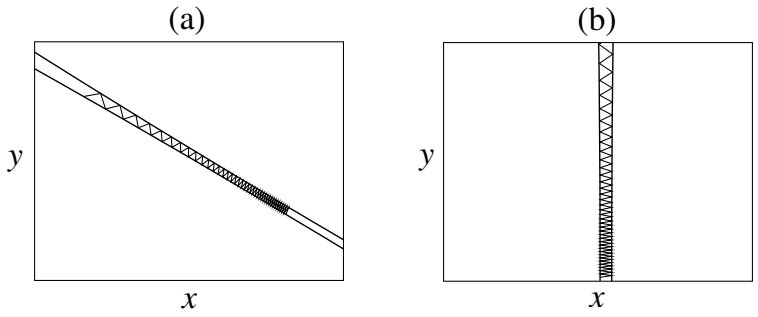

FIG. 28: Particle trapped between two disks very close to each other in the hexagonal geometry. The line joining their centers either (a) forms an angle with the horizontal or (b) is horizontal.

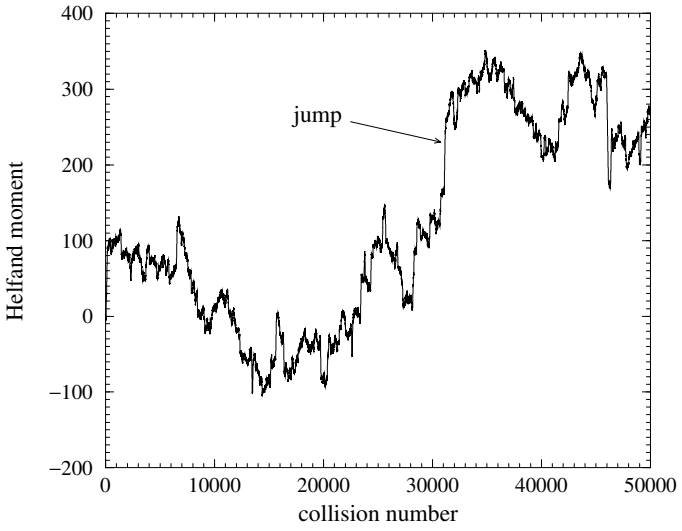

FIG. 29: Helfand moment in the hexagonal geometry evaluated along a particular trajectory at a density tending to the critical density.

VI. VISCOSITY IN SYSTEMS OF N HARD DISKS

In the present section, we apply our Helfand-moment method to systems of N hard disks. Our purpose is to show that the values of the shear viscosity obtained for the two-hard-disk model are in good agreement with the values for larger systems, as well as with Enskog's theory.

Figure 32 depicts the shear viscosity of systems containing from $N = 2$ up to $N = 40$ hard disks. For $N = 2$, we consider here the hexagonal geometry. For the systems with $N = 4$-40 disks, the time evolution is simulated by molecular dynamics with periodic boundary conditions in the square geometry. The viscosity is calculated by the Helfand-moment method based on Eq. (21).

We observe that, at low densities, the numerical values are in very good agreement between themselves. At higher densities, differences appear because the fluid-solid transition shifts toward higher densities as the number of disks increases. For $N = 2$ disks in the hexagonal geometry, the fluid-solid transition occurs in the interval $n = 0.57$-0.60, while it occurs in the interval $n = 0.87$-0.90 for $N = 40$. The sharp singularity of viscosity for $N = 2$ in the hexagonal geometry is specific to the geometrical constraints of a two-degree-of-freedom system, as explained in the previous section. Nevertheless, we notice that the decrease of the shear viscosity just above the fluid-solid transition is also the feature of the large system with $N = 40$ disks.

Furthermore, the results of our Helfand-moment method are compared with Enskog's theory. For a fluid of hard

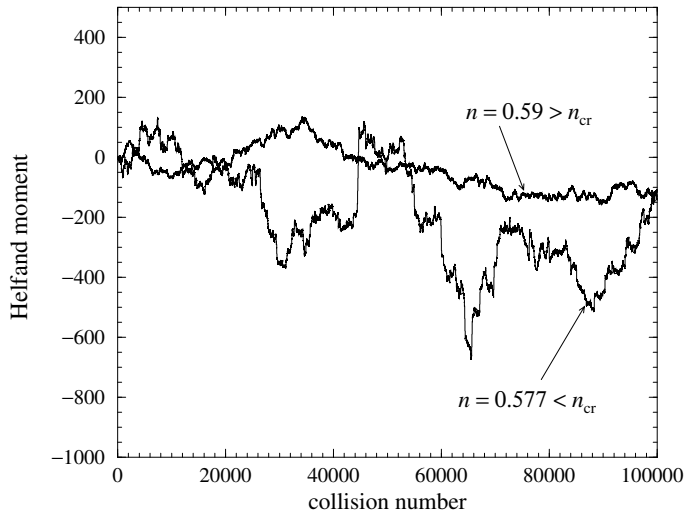

FIG. 30: Comparison of the evolution of the Helfand moment for two different densities separated by the critical density in the hexagonal geometry.

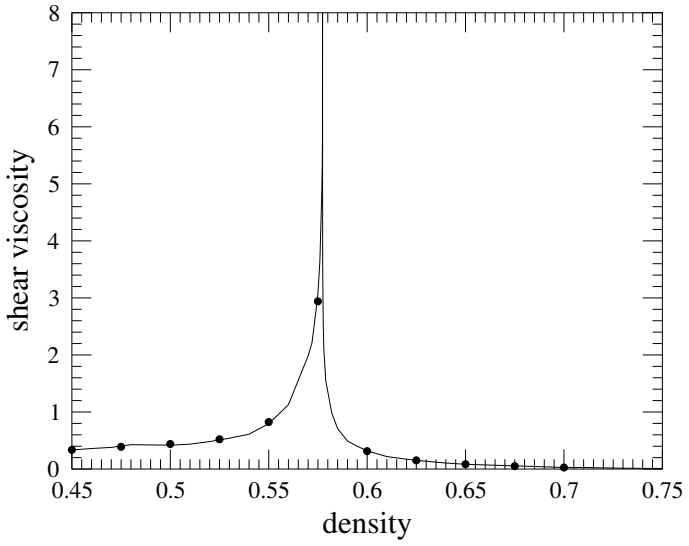

FIG. 31: Shear viscosity η^* in the hexagonal geometry calculated by our Helfand moment (16) (continuous line) and the one of Alder *et al.* (dots).

disks of mass m and diameter σ, Enskog's theory predicts that the shear viscosity is given by [18]

$$\eta = \eta_0 \left(\frac{1}{Y} + 2\,y + 3.4916\; Y\; y^2 \right) , \tag{68}$$

where

$$\eta_0 = \frac{1.022}{2\;\sigma} \sqrt{\frac{m\; k_{\rm B} T}{\pi}} . \tag{69}$$

is the Boltzmann value of the shear viscosity, Y is the Enskog factor entering the equation of state as follows:

$$P = n k_{\rm B} T (1 + 2\,y\; Y) . \tag{70}$$

and $y = \pi\sigma^2 n/4$. For the hard-disk fluid, a good approximation of the Enskog factor is given below the fluid-solid

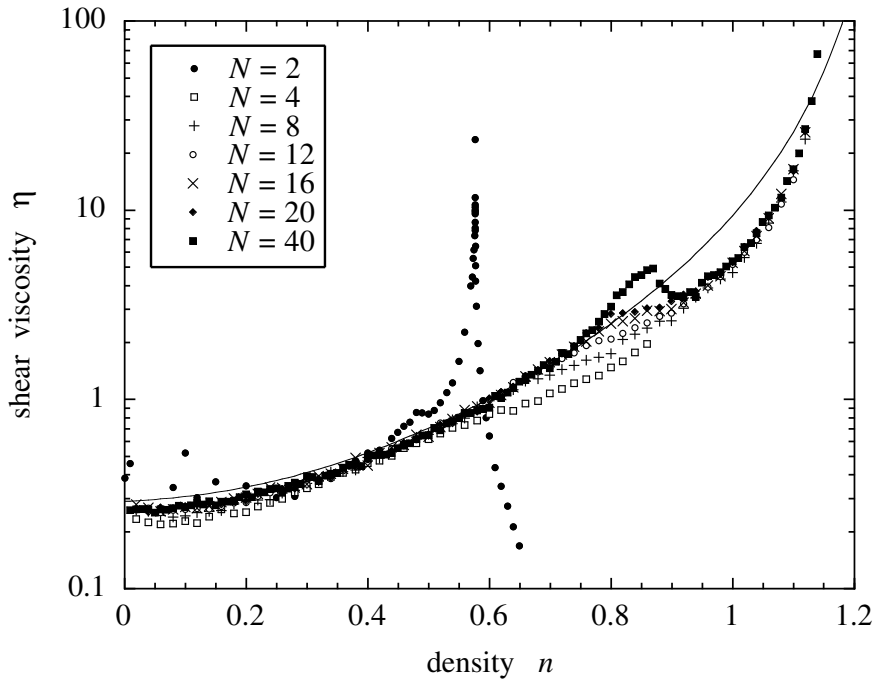

FIG. 32: Shear viscosity η versus particle density n in fluids at temperature $T = 1$ with $N = 2, 4, 8, 12, 16, 20, 40$ hard disks of unit mass and diameter. The solid line is Enskog's value (68). For $N = 2$, the data are the same as in Fig. 15 except that we here plot $\eta = 2\eta^*$ instead of η^* as in Fig. 15.

transition by [19]:

$$Y = \frac{1 - \frac{7}{16}\, y}{(1-y)^2} \,. \tag{71}$$

It is known that the Enskog approximation is not good around the fluid-solid transition and at very high densities.

A remark is here in order. It is known [20] that the viscosity coefficient of the infinite hard-disk fluid is diverging because of long-time tails. However, this divergence is only logarithmic and does not manifest itself in numerical calculations before extremely long times. This explains why the long-time tails do not spoil the agreement between the numerical values and Enskog's theory.

We see in Fig. 32 the good agreement between Enskog's theory and the numerical values of our Helfand-moment method at low densities showing the consistency of our results.

VII. CONCLUSIONS

In this paper, we propose a new expression for the Helfand moment associated with viscosity in molecular dynamics with periodic boundary conditions. This new Helfand moment takes into account the minimum image convention at the basis of molecular-dynamics simulations with periodic boundary conditions. In order to satisfy the minimum image convention, the position coordinates of the particles undergo jumps. These jumps modify both the equations of motion and the Helfand moment which is given by the time integral of the microscopic current entering the Green-Kubo formula. As a consequence, the viscosity tensor calculated with our Helfand moment is equivalent to the one based on the Green-Kubo formula, as proved in Appendix B. In the case of hard-ball systems, we also prove in Subsec. II D that our method is equivalent to the method by Alder *et al.* [6]. Moreover, we show in Appendix C that the hydrostatic pressure can also be calculated thanks to the Helfand moment we propose for molecular dynamics with periodic boundary conditions. Our new Helfand moment and our proofs bring a solution to the ambiguities and problems reported by Erpenbeck [9] about the definition of a Helfand moment in a molecular dynamics with periodic boundary conditions. We think that the Helfand-moment method can be very useful for the numerical calculation of viscosity because this method has the advantage of being numerically robust.

We have applied our Helfand-moment method to the numerical calculation of viscosity in systems of hard disks.

In Sec. V, viscosity has been studied in detail in a simple model composed of two hard disks in elastic collision. This model has already been investigated in the square geometry by Bunimovich and Spohn [10]. In the present paper, we generalize this model to the hexagonal geometry. First, we show that the fourth-order viscosity tensor is isotropic in the hexagonal geometry although it is not in the square geometry. Secondly, we show the viscosity can be positive and finite in the fluid phase of the hexagonal geometry, although it is always infinite in the fluid phase of the square geometry. The reason is that the horizon of the Sinai billiard driving the dynamics of the two-disk model is always infinite in the fluid phase of the square geometry although there is a regime with a finite horizon in the fluid phase of the hexagonal geometry. In an infinite-horizon regime, the viscosity becomes infinite so that, from a physical point of view, the proof of the existence of a positive and finite viscosity coefficient strictly holds in the hexagonal two-disk model. In the solid phase, the transport coefficients acquire a different meaning because the spontaneous breaking of translational invariance modifies the structure of the hydrodynamic modes and the viscosity coefficient should be reinterpreted in terms of the damping coefficients of the transverse sound modes and of the diffusive modes [21–23]. We hope to report on this question in a future publication.

The two-disk model presents a phase transition between a fluid and a solid phase. This transition is reminiscent of the fluid-solid transition in the system composed of many disks. Indeed, the transition manifests itself in the hydrostatic pressure in a very similar way as in the many-particle system. The hydrostatic pressure can be directly related to the mean free path in the two-disk model and we can thus explain the manifestation of the transition on the pressure in terms of the behavior of the mean free path near the transition. In this simple model, the transition can be understood as a geometrical property of the dynamical system. Indeed, the trajectories are unbounded in the fluid phase albeit there remain localized in bounded domains in the solid phase where ergodicity is broken. The fluid-solid transition also manifests itself as a diverging singularity in the viscosity in the two-disk model. We have here shown that this singularity in the viscosity versus the density may depend sensitively on the geometry of the lattice of the solid phase in formation.

In Sec. VI, we have extended the calculation of shear viscosity to systems with many disks. The remarkable result is that the two-disk systems already gives the shear viscosity in quantitative agreement with its values in larger systems, as well as with Enskog's theory at moderate densities.

In a companion paper, we report a study of viscosity by the escape-rate method [24]. In this other work, we use the Helfand moment which we have introduced in the present paper.

Acknowledgments. The authors thank Professors J. R. Dorfman and G. Nicolis for support and encouragement in this research. We also thank Dr. I. Claus for helpful discussions. SV thanks the Fund for the Education to the Research in Industry and Agriculture (FRIA) for financial support. PG thanks the National Fund for Scientific Research (FNRS Belgium) for financial support.

APPENDIX A: MICROSCOPIC DERIVATION OF THE VISCOSITY TENSOR

In this Appendix, we provide a short microscopic derivation of the viscosity tensor.

First, we need the balance equation for the local conservation of momentum. If we define the density of momentum as

$$g_i(\mathbf{r}) = \sum_{a=1}^{N} p_{ai}\, \delta(\mathbf{r} - \mathbf{r}_a)\ , \tag{A1}$$

the balance equation is

$$\partial_t\, g_i + \partial_j\, \tau_{ij} = 0\ , \tag{A2}$$

with $\partial_j = \partial/\partial r_j$. The microscopic momentum current density is given by

$$\tau_{ij} = \sum_{a=1}^{N} \frac{p_{ai}\, p_{aj}}{m}\, \delta(\mathbf{r} - \mathbf{r}_a) + \frac{1}{2} \sum_{a \neq b = 1}^{N} F_i(\mathbf{r}_a - \mathbf{r}_b) \int_0^1 d\lambda\, \frac{dr_{abj}}{d\lambda}\, \delta\left[\mathbf{r} - \mathbf{r}_{ab}(\lambda)\right]\ , \tag{A3}$$

where $\mathbf{r}_{ab}(\lambda)$ is the parametric equation of a curve joining the particles a and b: $\mathbf{r}_{ab}(0) = \mathbf{r}_b$ and $\mathbf{r}_{ab}(1) = \mathbf{r}_a$.

The microscopic current associated with viscosity is defined by integrating the momentum current density over the volume V:

$$J_{ij} = \int_V \tau_{ij}(\mathbf{r})\, d\mathbf{r}\ , \tag{A4}$$

which is given by Eq. (8). We notice that the hydrostatic pressure is given at equilibrium by

$$\langle J_{ij}\rangle_{\rm eq} = P\,V\,\delta_{ij}\;, \tag{A5}$$

if second-order tensors are isotropic in the system of interest.

We suppose that, at the initial time, the fluid is close to the equilibrium and described by the following nonequilibrium distribution:

$$\mathcal{P}(\Gamma) = \mathcal{P}_{\rm eq}(\Gamma)\left[1+\beta\int \mathbf{g}(\mathbf{r})\cdot\mathbf{v}(\mathbf{r})\,d\mathbf{r}\right] = \mathcal{P}_{\rm eq}(\Gamma)\left[1+\beta\sum_{a=1}^{N}\mathbf{p}_a\cdot\mathbf{v}(\mathbf{r}_a)\right]\;, \tag{A6}$$

where $\mathcal{P}_{\rm eq}$ is the equilibrium distribution and β is a normalization constant such that

$$\langle p_{ai}\,p_{bj}\rangle_{\rm eq} = \frac{m}{\beta}\,\delta_{ij}\,\delta_{ab}\;. \tag{A7}$$

In the microcanonical state, we have that

$$\beta = \frac{1}{k_{\rm B}T}\,\frac{N}{N-1}\;. \tag{A8}$$

The aforementioned distribution describes a fluid with a macroscopic velocity field $\mathbf{v}(\mathbf{r})$ since the nonequilibrium average of the momentum density can easily be shown to be given by

$$\langle \mathbf{g}(\mathbf{r})\rangle_{\rm noneq} = \rho_{\rm eq}\,\mathbf{v}(\mathbf{r})\;, \tag{A9}$$

where

$$\rho_{\rm eq} = m\,\frac{N}{V}\;, \tag{A10}$$

is the mass density at equilibrium.

The time evolution of the probability density (A6) is ruled by Liouville's operator given by the Poisson bracket with the Hamiltonian $\hat{L} = \{H,\cdot\}$ or the pseudo-Liouville operator in the case of hard-ball dynamics. This operator has the effect of replacing the phase-space coordinates Γ by $\Gamma(-t)$

$$\mathcal{P}_t = {\rm e}^{\hat{L}t}\mathcal{P}_0 = \mathcal{P}_{\rm eq}(\Gamma)\left[1+\beta\int {\rm e}^{\hat{L}t}\mathbf{g}(\mathbf{r})\cdot\mathbf{v}(\mathbf{r})\,d\mathbf{r}\right] = \mathcal{P}_{\rm eq}(\Gamma)\left[1+\beta\sum_{a=1}^{N}\mathbf{p}_a(-t)\cdot\mathbf{v}\left[\mathbf{r}_a(-t)\right]\right]\;. \tag{A11}$$

Alternatively, we known that the time evolution of the momentum density is given by Eq. (A2). In this case, the momentum density should be considered as an observable so that the solution of Eq. (A2) is

$$\mathbf{g}(\mathbf{r},t) = {\rm e}^{-\hat{L}t}\mathbf{g}(\mathbf{r},0)\;, \tag{A12}$$

so that

$${\rm e}^{\hat{L}t}\mathbf{g}(\mathbf{r}) = \mathbf{g}(\mathbf{r},-t)\;, \tag{A13}$$

is solution of the equation

$$\partial_t\,g_i = \partial_j\,\tau_{ij}\;. \tag{A14}$$

Integrating both sides over time we get

$$g_i(\mathbf{r},-t) = g_i(\mathbf{r},0) + \int_0^t dt'\;\partial_j\,\tau_{ij}(t')\;. \tag{A15}$$

Close to equilibrium, we may consider the time evolution of deviations with respect to the equilibrium. We neglect terms which are quadratic in the deviations such as the velocity field itself. The time evolution of these deviations is obtained by considering the nonequilibrium average of the balance equation (A2) for the deviations:

$$\partial_t\,\langle\delta g_i\rangle_{\rm noneq} + \partial_j\,\langle\delta\tau_{ij}\rangle_{\rm noneq} = 0\;, \tag{A16}$$

with

$$\delta\tau_{ij} = \tau_{ij} - \langle\tau_{ij}\rangle_{\rm eq} \; . \tag{A17}$$

The nonequilibrium average of the deviation of the momentum current density is given by

$$\langle\delta\tau_{ij}(\mathbf{r})\rangle_{\rm noneq} = \int \delta\tau_{ij}(\mathbf{r}) \; \mathcal{P}(\Gamma,t) \; d\Gamma = \beta \int d\mathbf{r}' \langle\delta\tau_{ij}(\mathbf{r}) \; g_k(\mathbf{r}',-t)\rangle_{\rm eq} \; v_k(\mathbf{r}') \; . \tag{A18}$$

We use Eq. (A15) to transform the average as

$$\langle\delta\tau_{ij}(\mathbf{r}) \; g_k(\mathbf{r}',-t)\rangle_{\rm eq} = \langle\delta\tau_{ij}(\mathbf{r}) \; g_k(\mathbf{r}',0)\rangle_{\rm eq} + \int_0^t dt' \; \langle\delta\tau_{ij}(\mathbf{r},0) \; \partial'_l \, \delta\tau_{kl}(\mathbf{r}',t')\rangle_{\rm eq} \; , \tag{A19}$$

where we have used the property that $\partial'_l\langle\tau_{kl}\rangle_{\rm eq} = 0$ because the equilibrium state is spatially uniform. We notice that the first term in the right-hand side of Eq. (A19) vanishes because the equilibrium average of an odd power of particle momenta vanishes. After an integration by part over the velocity field, Eq. (A18) becomes

$$\langle\delta\tau_{ij}(\mathbf{r})\rangle_{\rm noneq} = -\beta \int d\mathbf{r}' \int_0^t dt' \; \langle\delta\tau_{ij}(\mathbf{r},0) \; \delta\tau_{kl}(\mathbf{r}',t')\rangle_{\rm eq} \; \partial'_l v_k(\mathbf{r}') = -\eta_{ij,kl} \; \partial_l v_k(\mathbf{r}) \; , \tag{A20}$$

where the identification with the viscosity tensor is carried out in the limit $t \to \infty$ by

$$\eta_{ij,kl} \; \delta(\mathbf{r}-\mathbf{r}') = \beta \int_0^\infty dt' \; \langle\delta\tau_{ij}(\mathbf{r},0) \; \delta\tau_{kl}(\mathbf{r}',t')\rangle_{\rm eq} \; . \tag{A21}$$

Taking the double volume integral $\int_V d\mathbf{r} \int_V d\mathbf{r}'$ of both sides of Eq. (A21) and dividing by the volume V, we obtain the viscosity tensor as

$$\eta_{ij,kl} = \frac{\beta}{V} \int_0^\infty dt \; \langle\delta J_{ij}(0) \; \delta J_{kl}(t)\rangle_{\rm eq} \; , \tag{A22}$$

with

$$\delta J_{ij}(t) = \int_V d\mathbf{r} \; \delta\tau_{ij}(\mathbf{r},t) = J_{ij}(t) - \langle J_{ij}\rangle_{\rm eq} \; , \tag{A23}$$

Q.E.D.

APPENDIX B: PROOF OF THE EQUIVALENCE BETWEEN GREEN-KUBO AND EINSTEIN-HELFAND FORMULAS

Our aim is here to deduce the Green-Kubo formula (7) from the Einstein-Helfand formula (14), proving the equivalence between both formulas under the condition that the Helfand moment is defined by Eq. (15) as the time integral of the microscopic current (8) and the further condition that the time auto-correlation functions decrease fast enough.

We start from the Einstein-Helfand formula (14) with

$$\delta G_{ij}(t) = \int_0^t \delta J_{ij}(\tau) \; d\tau \; , \tag{B1}$$

δJ_{ij} being defined by Eq. (A23) and supposing for simplicity that $\delta G_{ij}(0) = 0$. Accordingly, we have successively from Eq. (14) that

$$\begin{aligned}
\eta_{ij,kl} &= \lim_{T\to\infty} \frac{\beta}{2TV} \; \langle\delta G_{ij}(T)\delta G_{kl}(T)\rangle \\
&= \lim_{T\to\infty} \frac{\beta}{2TV} \; \int_0^T dt_1 \int_0^T dt_2 \; \langle\delta J_{ij}(t_1)\delta J_{kl}(t_2)\rangle \\
&= \lim_{T\to\infty} \frac{\beta}{2TV} \; \int_{-T}^{+T} dt \int_{|t|/2}^{T-|t|/2} d\tau \; \langle\delta J_{ij}(0)\delta J_{kl}(t)\rangle
\end{aligned}$$

$$= \lim_{T\to\infty} \frac{\beta}{2V} \int_{-T}^{+T} dt \left(1 - \frac{|t|}{T}\right) \langle \delta J_{ij}(0) \delta J_{kl}(t) \rangle$$
$$= \frac{\beta}{2V} \int_{-\infty}^{+\infty} dt \, \langle \delta J_{ij}(0) \delta J_{kl}(t) \rangle$$
$$= \frac{\beta}{V} \int_{0}^{+\infty} dt \, \langle \delta J_{ij}(0) \delta J_{kl}(t) \rangle \, , \tag{B2}$$

where we have performed the change of integration variables

$$\begin{cases} t = t_2 - t_1 \, , \\ \tau = \frac{t_1 + t_2}{2} \, , \end{cases} \tag{B3}$$

and supposed that

$$\lim_{T\to\infty} \frac{1}{T} \int_{-T}^{+T} dt \, |t| \, \langle \delta J_{ij}(0) \delta J_{kl}(t) \rangle = 0 \, , \tag{B4}$$

which requires that the time autocorrelation functions decrease faster than $|t|^{-1-\epsilon}$ with $\epsilon > 0$. Q.E.D.

APPENDIX C: PRESSURE AND HELFAND MOMENT

The hydrostatic pressure at equilibrium is given as the mean value of the momentum current density, i.e., as the mean value of the same microscopic current entering the Green-Kubo relation:

$$P_{ij} V = \int_V \langle \tau_{ij} \rangle_{\rm eq} \, d\mathbf{r} = \langle J_{ij} \rangle_{\rm eq} \, . \tag{C1}$$

The average over the thermodynamic equilibrium state can be replaced by a time average:

$$P_{ij} V = \langle J_{ij} \rangle_{\rm eq} = \lim_{t\to\infty} \frac{1}{t} \int_0^t d\tau \, J_{ij} \, . \tag{C2}$$

We can here introduce the Helfand moment to obtain the hydrostatic pressure from the Helfand moment as:

$$P_{ij} V = \lim_{t\to\infty} \frac{1}{t} \left[G_{ij}(t) - G_{ij}(0) \right] \, . \tag{C3}$$

In the microcanonical equilibrium state we have that

$$\langle p_{ai} \, p_{aj} \rangle_{\rm eq} = m \, k_{\rm B} T \, \frac{N-1}{N} \, \delta_{ij} \, . \tag{C4}$$

If we assume that the system is isotropic, $P_{ij} = P \, \delta_{ij}$ and we obtain

$$PV = (N-1) k_{\rm B} T + R \, , \tag{C5}$$

where the rest R provides the corrections to the law of perfect gases in dense systems. By using Eqs. (16) and (21), the virial can be computed alternatively by

$$R = \left\langle \frac{1}{2d} \sum_{a\neq b=1}^{N} \mathbf{F}(\mathbf{r}_{ab}) \cdot \mathbf{r}_{ab} \right\rangle_{\rm eq} \tag{C6}$$
$$= \lim_{t\to\infty} \frac{-1}{td} \sum_s \sum_{a=1}^{N} \mathbf{p}_a^{(s)} \cdot \Delta \mathbf{r}_a^{(s)} \, \theta(t - t_s) \tag{C7}$$
$$= \lim_{t\to\infty} \frac{1}{td} \sum_c \Delta \mathbf{p}_a^{(c)} \cdot \mathbf{r}_{ab}^{(c)} \, \theta(t - t_c) \tag{C8}$$

where d is the dimension, $\mathbf{r}_{ab} = \mathbf{r}_a - \mathbf{r}_b$, t_s are the times of jumps to satisfy the minimum image convention, while the last expression only holds for hard-ball systems, t_c are the collision times, and $\mathbf{r}_{ab}^{(c)} = \mathbf{r}_a(t_c) - \mathbf{r}_b(t_c)$.

---

[1] M. S. Green, J. Chem. Phys. **19**, 1036 (1951).
[2] M. S. Green, Phys. Rev. **119**, 829 (1960).
[3] R. Kubo, J. Phys. Soc. Jpn. **12**, 570 (1957).
[4] H. Mori, Phys. Rev. **112**, 1829 (1958).
[5] E. Helfand, Phys. Rev. **119**, 1 (1960).
[6] B. J. Alder, D. M. Gass, and T. E. Wainwright, J. Chem. Phys. **53**, 3813 (1970).
[7] A. A. Chialvo and P. G. Debenedetti, Phys. Rev. A **43**, 4289 (1991).
[8] M. P. Allen, in M. P. Allen and D. J. Tildesley (Eds.), *Computer Simulation in Chemical Physics* (Kluwer, Amsterdam, 1993) 49-92.
[9] J. J. Erpenbeck, Phys. Rev. E **51**, 4296 (1995).
[10] L. A. Bunimovich and H. Spohn, Comm. Math. Phys. **176**, 661 (1996).
[11] L. D. Landau and E. M. Lifshitz, *Fluid Mechanics* (Addison-Wesley, Reading MA, 1981).
[12] R. Aris, *Vectors, Tensors and the Basic Equations of Fluid Mechanics* (Prentice-Hall Inc., Englewood Cliff NJ, 1962).
[13] D. A. McQuarrie, *Statistical Mechanics* (Harper & Row, New York, 1976) Chap. 21.
[14] P. Gaspard, *Chaos, Scattering and Statistical Mechanics* (Cambridge University Press, Cambridge UK, 1998).
[15] Ya. G. Sinai, Russ. Math. Survey **25**, 181 (1975).
[16] L. A. Bunimovich and Ya. G. Sinai, Comm. Math. Phys. **78**, 247, 479 (1980).
[17] J. Machta and R. Zwanzig, Phys. Rev. Lett. **50**, 1959 (1983).
[18] D. M. Gass, J. Chem. Phys. **54**, 1898 (1971).
[19] J. A. Barker and D. Henderson, Rev. Mod. Phys. **48**, 587 (1976).
[20] B. J. Alder and T. E. Wainwright, Phys. Rev. Lett. **18**, 988 (1967); J. R. Dorfman and E. G. D. Cohen, Phys. Rev. Lett. **25**, 1257 (1970); M. H. Ernst, E. H. Hauge, and J. M. van Leeuwen, Phys. Rev. A **4**, 2055 (1971).
[21] P. C. Martin, O. Parodi, and P. S. Pershan, Phys. Rev. A **6**, 2401 (1972).
[22] P. D. Fleming III and C. Cohen, Phys. Rev. B **13**, 500 (1976).
[23] T. R. Kirkpatrick, S. P. Das, M. H. Ernst, and J. Piasecki, J. Chem. Phys. **92**, 3768 (1990).
[24] S. Viscardy and P. Gaspard, *Viscosity in the escape-rate formalism*, preprint `cond-mat/0309432`, Phys. Rev. E **68** (2003).